Land Surface Temperature and Urban Heat Island Dynamics from 2010 to 2018 Using Landsat Imagery in an Arid Environment: A Case Study in Sunland Park, New Mexico, USA

Tawalbeh, Z. M.
Department of Civil Engineering, Faculty of Engineering, Ajloun National University, P.O. Box 43, Ajloun 26810, Jordan, E-mail: z.tawalbeh@anu.edu.jo

DOI: https://doi.org/10.52939/ijg.v22i8.5143

Abstract
Urbanization significantly impacts land surface temperature (LST) and the characteristics of urban heat islands (UHI). However, the relationship between these factors can be complex, particularly in arid regions where exposed soils and sparse vegetation can lead to exceptionally high daytime temperatures. This study explores how changes in land use and land cover (LULC) related to urbanization affect LST, vegetation conditions, and UHI characteristics in Sunland Park, New Mexico. We analyzed five cloud-free Landsat images from the Landsat-5 TM and Landsat-8 OLI/TIRS satellites, captured in May during the years 2010, 2011, 2013, 2016, and 2018. To map LULC changes, we employed supervised maximum likelihood classification, while the Normalized Difference Vegetation Index (NDVI), emissivity-corrected LST, and a normalized UHI index were calculated to assess daytime thermal patterns on the surface. The overall accuracy of the classification ranged from 85% to 87%, with Kappa coefficients between 0.74 and 0.78. Over the study period, we observed an increase in urban land from 7.53 km² to 12.23 km², alongside a decrease in rangeland from 17.82 km² to 12.30 km². Our analysis indicated that the highest daytime LST values and the most intense UHI effects were typically linked to exposed barren land and sparsely vegetated rangelands. Notably, certain urban zones experienced lower LST than adjacent barren areas. A significant inverse relationship between NDVI and LST ($R^2 = 0.60$–0.80) highlighted the cooling effects of vegetation, largely attributed to shading and evapotranspiration. These findings suggest that daytime thermal conditions in arid areas are shaped not only by the expansion of urban areas but also by the specific characteristics of the land being converted and the land management practices that follow. It is important to note that this analysis, based on five selected Landsat scenes from May, should be considered reflective of the specific acquisition dates rather than indicative of year-round thermal behavior or a general trend that urbanization decreases surface temperatures in arid environments.

Keywords: Arid Environment, Land Surface Temperature (LST), NDVI, Urban Heat Island (UHI), Urbanization

1. Introduction

The United States of America (USA) developed its urban areas through multiple development methods that spread across different spatial areas at various scales since the nineteenth century [1]. The process of urbanization involves the conversion of natural areas and rural territories into urban areas because of increasing population numbers and economic expansion [2]. Urbanization continues as an unavoidable process which produces negative environmental effects that damage land surfaces and create desert areas while raising water consumption and eliminating rural farming areas [3]. Urbanization leads to the replacement of natural land surfaces (vegetation, exposed soil and surface water) with impervious materials (concrete/asphalt/metal structures), resulting in significant changes to surface biophysical characteristics [1].

The process of turning vegetated areas into urban spaces creates multiple effects which impact surface energy balance, land surface temperature (LST), water quality, ecosystem services and biodiversity, and human health [4]. The construction of buildings on natural landforms results in higher sensible heat flux and surface temperature which produces the urban heat island (UHI) effect [5].

ISSN: 1686-6576 (Printed) | ISSN 2673-0014 (Online) |

Multiple remote sensing-based classification methods need to evaluate these changes by analyzing multispectral and hyperspectral data through maximum likelihood classification (MLC), support vector machines, and neural networks [6]. The process of image classification requires researchers to establish suitable classification methods and choose training data and then they must use ground reference information to verify their results [7]. In addition, several change detection approaches such as image differencing, principal component analysis, and post-classification comparison have been widely used to quantify land use and land cover (LULC) dynamics [8], particularly in arid and semi-arid environments [9].

Considerable attention has been given to the relationship between LULC changes and local climate variability, especially regarding the development of the urban heat island effect. The definition of UHI indicates how urban areas become hotter than rural areas because of human actions which change land surfaces. Scientists need to start studying right away how UHI affects human health and how it affects both ecosystems and weather patterns and climate systems [10]. The study of UHI requires scientists to measure air temperatures directly at particular sites or they can use satellite thermal infrared data to determine land surface temperatures [11]. Remote sensing techniques allow scientists to track urban areas throughout time because they effectively monitor Urban Heat Island (UHI).

Vegetation functions as a temperature controller for surfaces because it uses evapotranspiration to cool down and creates shade to lower temperatures. Numerous studies have demonstrated that increasing urban vegetation through green infrastructure including urban forests, parks, green roofs, and vegetated corridors is among the most effective strategies for mitigating urban heat island effects. Vegetation reduces surface and near-surface temperatures primarily through evapotranspiration, shading, and modification of the surface energy balance, thereby improving thermal comfort and reducing building cooling demands. A comprehensive review has shown that green roofs can significantly reduce surface temperatures while providing additional environmental benefits, including improved stormwater management, energy conservation, and enhanced urban sustainability [12]. Similar conclusions have been reported in subsequent studies, confirming that integrating vegetation into urban environments represents an effective climate adaptation strategy for reducing heat stress and improving urban resilience [12][13] and [14].

Research studies have employed the Normalized Difference Vegetation Index (NDVI) to assess vegetation density during their investigations of LST responses to various land cover types [15] and [16]. Multiple studies demonstrate that NDVI shows a strong connection to LST, but vegetation fraction produces a more powerful relationship between these variables which operate across various spatial scales and different land cover types [16]. Empirical investigations have consistently demonstrated a negative relationship between NDVI and LST in urban environments [17]. However, in arid environments such as Sunland Park, the relationship between soil temperature and solar radiation becomes more complex because the sandy ground responds strongly to temperature fluctuations with low thermal inertia (heat up and cool down quickly). In contrast to humid regions, where built-up areas tend to be the hottest, barren rangelands achieve radiative equilibrium more quickly than concrete or asphalt structures under intense sunlight. As a result, urban environments may act as thermal shields: buildings provide shade, and irrigation supports vegetation that helps keep surface temperatures lower than those in the surrounding desert landscape. This suggests that urban expansion in dry areas may present a unique opportunity for thermal regulation if it is managed through strategic shading and the use of native vegetation.

The process of urbanization and LULC change requires land surface temperature measurements which need to be precise for thermal impact assessment. Multiple retrieval algorithms have been developed to retrieve LST from satellite thermal data through mono-window, single-channel, split-window, and temperature/emissivity separation methods [18] [19] and [20]. The methods used to retrieve LST data take into account three essential elements which affect the precision of the results: land surface emissivity, atmospheric conditions, and sensor operating parameters [16]. Advances in satellite remote sensing and geographic information systems have enabled efficient analysis of long-term spatial and temporal patterns of surface temperature and urban expansion [1].

Research about urbanization and UHI has produced many studies, but these investigations maintain that cities grow through processes which raise local surface temperatures. The assumption does not always apply to arid regions because their surface temperatures in exposed soil and degraded rangelands tend to be higher than those in built-up areas. The current scientific literature lacks studies which investigate how urbanization impacts LST measurement results in these environmental settings. This work investigates the impact of urbanization on land use and land cover patterns, NDVI values, LST readings, and the development of urban heat islands (UHI) in Sunland Park, New Mexico, USA. This analysis utilizes Landsat satellite data from 2010 to 2018. The study aims to examine how urbanization in dry areas affects ground temperature patterns compared to regions with more vegetation. Additionally, it seeks to provide valuable insights for sustainable urban planning and land use in arid cities.

2. Materials and Methods

2.1 Study Area

Figure 1 shows the location of the study area, the City of Sunland Park, which is an 11.6 square mile ($30\ km^2$) area. The area is known historically as Anapra and is situated in the Rio Grande Valley in southern Doña Ana County, New Mexico. Sunland Park borders its international neighbor Texas to the east and the Mexican state of Chihuahua to the south. Its location places it in the immediate vicinity of El Paso, Texas, and Ciudad Juárez, Mexico, which are two of the largest metropolitan areas in the United States and Mexico respectively. Sunland Park is characterized by a predominantly arid desert climate. It receives less than 9.2 inches of annual rainfall and experiences high annual solar insolation. The surrounding environment supports vegetation typical of the Chihuahuan Desert, including mesquite trees, creosote bushes, and various cactus species [21]. The city has an average elevation of 3,789 feet (1,152 m) above mean sea level and is located at latitude $31°48'24''$N and longitude $106°34'48''$W ($31.8067°$N, $-106.5800°$W). The Rio Grande, which starts in Colorado, flows right through Sunland Park, serving as the primary watercourse for the study area. Figure 2 presents the consistent population growth in Sunland Park throughout the study period. While population data were not explicitly included in the remote sensing analysis, the documented increase supports the findings of urban expansion revealed by the Landsat-derived land use and land cover (LULC) maps. In particular, the rise in urban land area from 2010 to 2018 aligns with ongoing residential and infrastructure development linked to population growth. As such, population data serves as contextual information rather than a variable utilized in quantitative thermal analysis.

According to the 2010 U.S. Census, Doña Ana County saw a significant population boost of nearly 20% between 2000 and 2010. Much of this growth was driven by the City of Sunland Park and the Las Cruces metropolitan region [22]. Subsequent data indicates that Sunland Park's population increased from 13,309 to 15,588 between 2000 and 2016 (Figure 2). While the city continues to grow, its population density remains lower than nearby regional centers such as Las Cruces, Albuquerque, and El Paso, which reported populations of approximately 101,459, 556,859, and 678,058 residents, respectively. The population information is presented as background to describe the general development of the city and is not used directly in the quantitative analysis of land use/land cover change or land surface temperature.

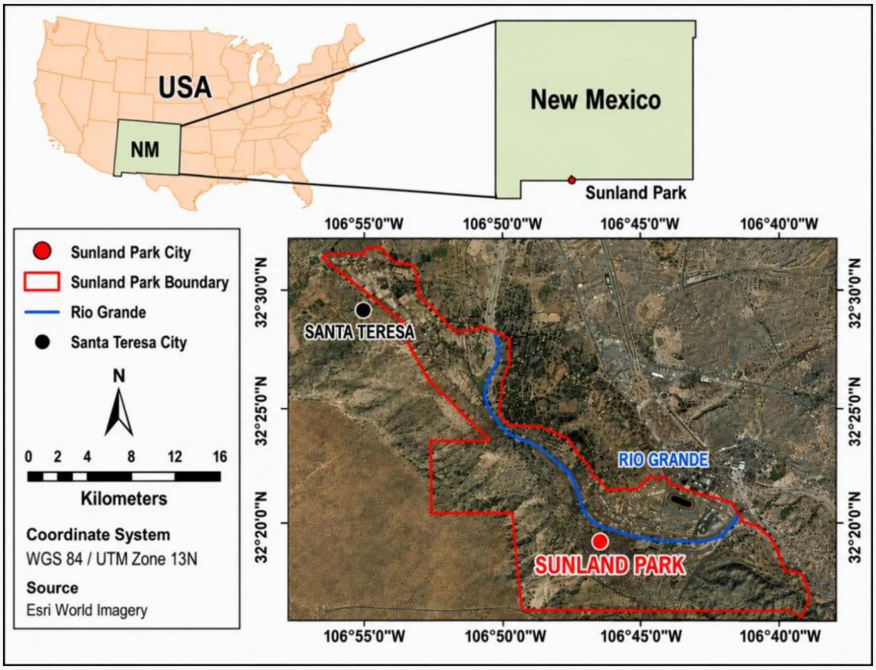

Figure 1: Sunland Park, New Mexico, USA

ISSN: 1686-6576 (Printed) | ISSN 2673-0014 (Online) | © Geoinformatics International

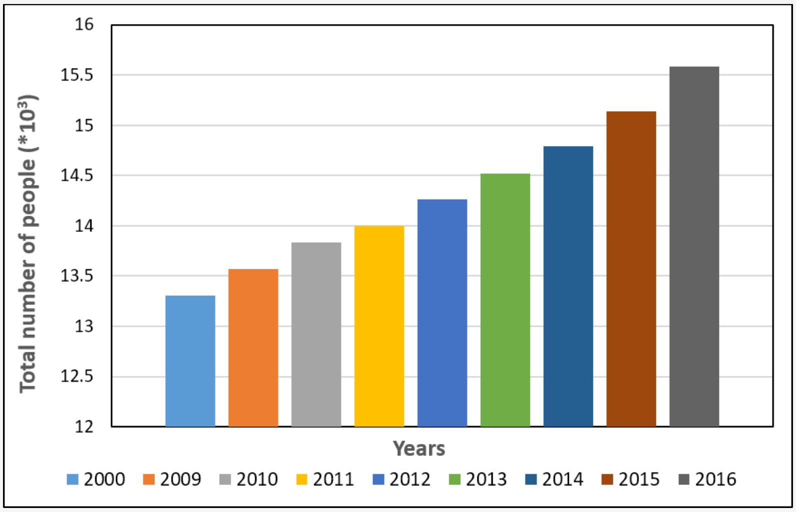

Figure 2: Population development at Sunland Park, NM from 2000 to 2016 [23]

Table 1: Metadata information for the selected Landsat images used in this study

Year	Satellite Path/Row	Sensor	Acquisition Date	Landsat IDs	Acquisition Time (UTC)	Cloud Cover (%)	Product Level	Sun Elev. (°)	Sun Azim. (°)	Thermal Band(s) Used
2010	Landsat-5 033/038	TM	13 May 2010	LT50330382010133EDC00	17:30:28	0.00	L1TP	65.22	116.81	Band 6
2011	Landsat-5 033/038	TM	16 May 2011	LT50330382011136PAC01	17:29:15	2.00	L1TP	65.37	115.13	Band 6
2013	Landsat-8 033/038	OLI/TIRS	21 May 2013	LC80330382013141LGN02	17:41:43	0.00	L1TP	68.40	116.95	Bands 10 & 11
2016	Landsat-8 033/038	OLI/TIRS	13 May 2016	LC80330382016134LGN01	17:39:13	0.04	L1TP	66.96	119.72	Bands 10 & 11
2018	Landsat-8 033/038	OLI/TIRS	19 May 2018	LC80330382018139LGN00	17:38:39	0.00	L1TP	67.57	116.84	Bands 10 & 11

2.2 Image Acquisition and Processing

Five Landsat-5 Thematic Mapper (TM) and Landsat-8 Operational Land Imager/Thermal Infrared Sensor (OLI/TIRS) images with minimal cloud cover (0–2%), acquired in May of 2010, 2011, 2013, 2016, and 2018, were obtained from the U.S. Geological Survey (USGS) Earth Explorer platform [24]. All images were provided as Level-1 Terrain Precision (L1TP) products in GeoTIFF format and were referenced to the Universal Transverse Mercator (UTM) coordinate system (Zone 13 North, WGS 1984 datum). The metadata for the selected images, including acquisition date, acquisition time, cloud cover, sun elevation, sun azimuth, thermal bands, and processing level, are summarized in Table 1.

Landsat-5 TM and Landsat-8 OLI/TIRS images were acquired during the same seasonal period (May) to minimize the influence of seasonal variability on land cover and surface temperature comparisons. All scenes correspond to the Worldwide Reference System-2 (WRS-2) Path 033 and Row 038 and fully cover the study area. The reflective and thermal bands from both sensors were used for land use/land cover classification and land surface temperature retrieval, respectively. The reflective (multispectral) bands have a spatial resolution of 30 m, which enables effective identification of surface features and has been widely demonstrated to be suitable for land use and land cover mapping and monitoring applications [25]. Whereas the thermal bands have native spatial resolutions of 120 m for Landsat-5 TM and 100 m for Landsat-8 TIRS. In the Level-1 products, the thermal bands were provided resampled to 30 m by the USGS; therefore, no additional spatial resampling was required during image preprocessing. The images were selected because of their minimal cloud cover (0–2%), consistent seasonal acquisition, and suitability for reliable multi-temporal comparison. Because Landsat imagery is acquired during daytime satellite

ISSN: 1686-6576 (Printed) | ISSN 2673-0014 (Online) |

overpasses, the LST analyses presented herein represent daytime land surface temperature conditions only and do not characterize nighttime urban heat island behavior. Detailed information on band designations, spectral ranges, and spatial resolutions is provided in Table 2.

Although atmospheric correction is not strictly required for image classification when applying the maximum likelihood classifier to single-date imagery [26], most recent studies recommend its application to improve data consistency and comparability. Accordingly, all spectral bands used in this work were atmospherically corrected using the radiometric calibration tools in the Environment for Visualizing Images (ENVI®5.5) software. Digital number (DN) values were first converted to top-of-atmosphere (TOA) reflectance, after which surface reflectance was derived using the dark-object subtraction (DOS) method [27]. Among image-based atmospheric correction techniques, the DOS method was selected based on the assumption proposed by Chavez [28] that some pixels within an image correspond to dark objects whose recorded radiance is primarily due to atmospheric scattering rather than surface reflectance. In practice, truly dark objects with zero reflectance are rare; therefore, assuming a minimum reflectance value of approximately 1% is considered more realistic than assuming zero reflectance [28][29][30] and [31]. This approach allows for more accurate correction of atmospheric effects, particularly those caused by haze and scattering.

Converting raw digital numbers into reflectance values is important for getting accurate surface information. This process helps minimize the impact of atmospheric conditions and variations in radiometry when comparing images taken at different times [28]. Due to its simplicity and effectiveness, the DOS method has been widely applied in land use/land cover classification and change detection studies [32]. While more advanced atmospheric correction products, such as Landsat Collection 2 Surface Reflectance, are available, they provide significant improvements in radiometric calibration, geometric accuracy, and processing consistency through standardized Level-1 and Level-2 science products designed for long-term Earth observation analyses [33]. Nevertheless, the Dark Object Subtraction (DOS) method was adopted in this study to ensure a consistent preprocessing workflow for both Landsat-5 TM and Landsat-8 OLI/TIRS imagery. This choice was made because DOS offers a reliable and computationally efficient preprocessing technique for analyzing multi-temporal images. All the selected Landsat scenes were gathered in May and experienced minimal cloud cover (0–2%), which helped mitigate the effects of seasonal and atmospheric variability. However, it's important to note that DOS is a simplified atmospheric correction approach and might not address all atmospheric influences, especially under more variable acquisition conditions. Additionally, thermal atmospheric correction was executed separately during the retrieval of land surface temperature, utilizing sensor-specific methods that were distinct from the optical atmospheric correction applied to the reflective bands.

Table 2: Spectral characteristics and spatial resolutions of the Landsat-5 TM and Landsat-8 OLI/TIRS bands used in this study

Satellite	Band Name	Bandwidth (µm)	Resolution (m)
Landsat-5	Band 1 Blue	0.45 – 0.52	30
	Band 2 Green	0.52 – 0.60	30
	Band 3 Red	0.63 – 0.69	30
	Band 4 NIR	0.76 – 0.90	30
	Band 5 SWIR 1	1.55 – 1.75	30
	Band 7 SWIR 2	2.08 – 2.35	30
	Band 6 TIR	10.40 – 12.50	120 (resampled to 30)
Landsat-8	Band 1 Coastal	0.43 – 0.45	30
	Band 2 Blue	0.45 – 0.51	30
	Band 3 Green	0.53 – 0.59	30
	Band 4 Red	0.64 – 0.67	30
	Band 5 NIR	0.85 – 0.88	30
	Band 6 SWIR 1	1.57 – 1.65	30
	Band 7 SWIR 2	2.11 – 2.29	30
	Band 8 Pan	0.50 – 0.68	15
	Band 9 Cirrus	1.36 – 1.38	30
	Band 10 TIRS 1	10.6 – 11.19	100 (resampled to 30)
	Band 11 TIRS 2	11.5 – 12.51	100 (resampled to 30)

A schematic overview of the complete methodological framework employed in this analysis, from image acquisition to the derivation of biophysical parameters (NDVI, LST, and UHI), is presented in Figure 3 (Section 2.3).

2.3 Methodology Flowchart

As illustrated in Figure 3, the Landsat imagery was first separated according to sensor type to account for differences between Landsat-5 TM and Landsat-8 OLI/TIRS. The reflective bands were atmospherically corrected using the Dark Object Subtraction (DOS) method and subsequently used for LULC classification and NDVI calculation. For Landsat-5, the thermal infrared data were converted from digital numbers to TOA radiance and then to brightness temperature, while surface emissivity was estimated using the NDVI-threshold method. For Landsat-8, the thermal bands were processed using the Normalized Emissivity Method/Temperature Emissivity Separation (NEM/TES) approach for emissivity and temperature estimation. The retrieved LST products were then used to calculate the UHI index, while NDVI was retained for subsequent analysis of the relationship between vegetation conditions and surface temperature.

2.4 Image Classification

The classification scheme used in this analysis was developed to address the present work objectives related to urbanization and its influence on land surface temperature (LST) in Sunland Park. Based on these research objectives, the study area was classified into five main land use/land cover (LULC) classes: urban, vegetation, rangeland, barren land, and water. A detailed description of each class and its characteristics is provided in Table 3. Various classification schemes have been proposed for land use and land cover mapping; however, the U.S. Geological Survey Land-Use and Land-Cover Classification System (USGS LULC) presented in [34] has become a widely used framework for land-cover classification. The framework has become the most popular method which organizations use for strategic planning. The USGS LULC system bases its classification on land cover elements instead of human activities because it serves as a tool for analyzing remotely sensed information. Accordingly, the classification scheme adopted in this work follows the general structure of the USGS LULC system while being adapted to reflect the specific environmental and urban characteristics of the study area.

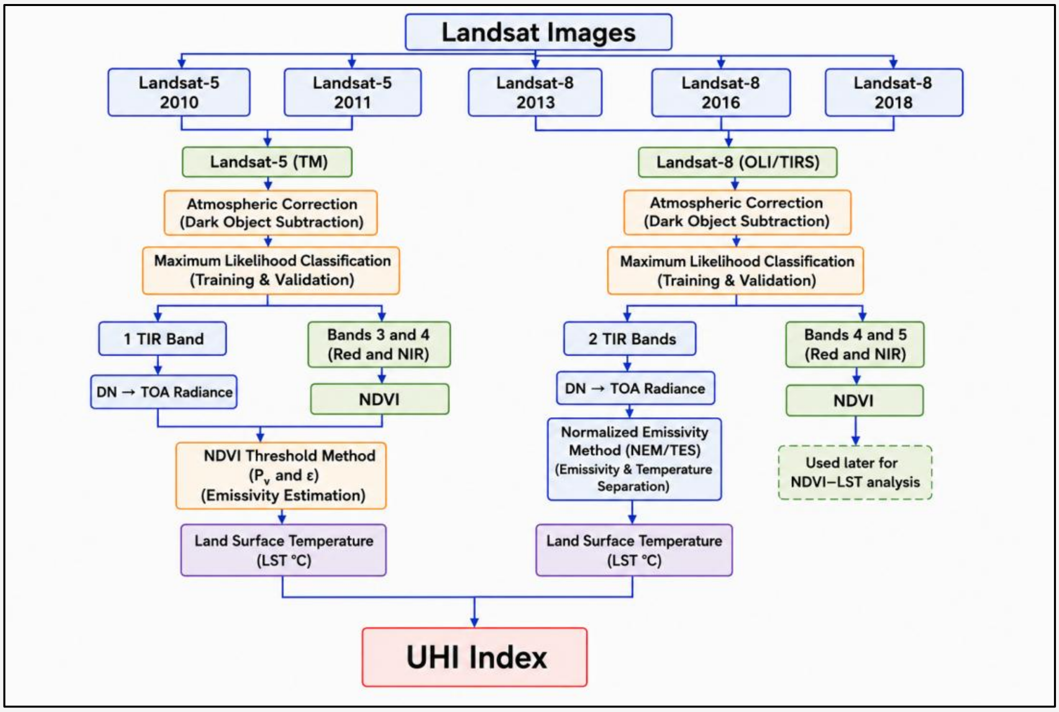

Figure 3: Methodological workflow for Landsat image processing, Maximum Likelihood classification, NDVI calculation, LST retrieval, and UHI analysis

ISSN: 1686-6576 (Printed) | ISSN 2673-0014 (Online) | © Geoinformatics International

Table 3: General description of level I classes [34]

Level I Class*	Description
Urban (Built-up Land)	Area of intensive use covered by structures, including cities, towns, villages, strip developments along highways, transportation, shopping centers, industrial and commercial complexes and institutions.
Vegetation (Agricultural Land)	Vegetated areas consisting primarily of irrigated agricultural land along the Rio Grande floodplain. In the study area, vegetation is dominated by cultivated fields sustained through irrigation because of the limited natural precipitation.
Rangeland	Mix of herbaceous rangeland species of the Chihuahuan Desert. It is a highly heterogenous class where the natural vegetation are shrubs and grasses.
Water	Area that represents the water body covering the area of interest. In our study it will include the river (Rio Grande).
Barren Land	Area of limited ability to support life in which less than one-third of the surface has vegetation or other cover. It represents soil, sand, or rocks exposed due to vegetation removal and human activity.

The images were classified in ArcGIS using supervised maximum likelihood classification (MLC), while ENVI® 5.5 was used for spectral-signature analysis and preprocessing. The USDA Cropland Data Layer (CDL) was used only as a supplementary reference [35] during the interpretation of land cover classes and the selection of representative training samples, particularly for Vegetated areas. It was not used as the primary validation dataset for the classification results. The final land use/land cover maps were evaluated using an independent accuracy assessment based on reference samples interpreted from high-resolution Google Earth imagery, and classification performance was quantified using confusion matrices, overall accuracy, producer's accuracy, user's accuracy, and the Kappa coefficient. The accuracy assessment results are presented in Section 3.3. In this classifier (MLC), the normal probability distributions for each of the spectral classes were arranged in a covariance matrix by selecting several pixels for each spectral class as training samples for the classification algorithm [7]. For this purpose, MLC maps were generated from the selected May Landsat scenes for 2010, 2011, 2013, 2016, and 2018.

Training sample sizes were determined following the commonly applied rule of thumb of at least ten times the number of spectral bands per class [36]. They were manually selected from homogeneous land-cover areas using high-resolution Google Earth imagery together with the USDA Cropland Data Layer as reference sources. Independent training datasets were prepared separately for each study year to account for temporal variations in land cover and spectral response. The number of training ROIs varied among land-cover classes according to their spatial extent and spectral heterogeneity within the study area. Table 4 summarizes the number of training ROIs used for each land-cover class and study year. Training samples were spatially distributed throughout the study area while avoiding adjacent or overlapping samples to minimize spatial autocorrelation.

The supervised Maximum Likelihood Classifier (MLC) implemented in ArcGIS was applied using the default classifier parameters. Prior to classification, the statistical separability of the training ROIs was evaluated using the spectral signature analysis tools available in ENVI®5.5 to verify adequate spectral discrimination among land-cover classes. The MLC assumes a normal distribution of spectral responses within each class and assigns each pixel to the class with the highest posterior probability based on the class mean vectors and covariance matrices. The study area received its training samples through a distribution method which aimed to place them across the entire study area while preventing the selection of adjacent or neighboring pixels [37]. Training data were collected independently for each year to account for temporal variations in land cover and spectral response. The areal extent of each land cover class in the classified images was subsequently calculated using direct pixel counts within the ArcGIS environment.

Table 4: Number of training data collected for each land cover class

Year	Urban	Vegetation	Range Land	Water	Barren
2010	90	35	82	20	11
2011	140	30	60	19	15
2013	80	12	55	20	9
2016	70	10	50	19	7
2018	99	15	45	32	10

2.5 Change Detection on the Earth's Surface

The post-classification change detection approach was chosen for this assessment because it effectively analyzes the magnitude and spatial distribution of land cover changes, including both gains and losses within individual classes. This method allows for direct comparisons between independently classified maps and is especially useful for identifying specific transitions between classes over time. Post-classification change detection was applied to the land use/land cover maps generated for the years 2010 and 2018. Change detection percentages were calculated for all land cover classes, including urban, vegetation, rangeland, barren land, and water, to quantify the extent and direction of land cover transformations within the study area.

2.6 Classification accuracy assessment

The evaluation of classification accuracy requires a statistically valid sampling approach to determine if the assigned land use or land cover class matches the actual ground conditions of each pixel [38]. This analysis used a GIS system to create random reference points which were then exported to KMZ format from classified maps. The evaluation of reference points used Google Earth Pro images which were synchronized with Landsat classified data from the same time period to establish a unified timeline that enhanced the assessment accuracy [39]. The interpreted reference data were then used to populate the error (confusion) matrices for accuracy evaluation.

A total of 300 reference points were used to assess the classification accuracy for each year, following the rule of thumb proposed by Jensen [36], which recommends using a number of reference samples equivalent to at least ten times the number of spectral bands per class. Given six spectral bands and five land cover classes, 300 reference points per classified image were considered sufficient to produce reliable accuracy estimates. For each of the classified maps, a confusion (error) matrix was constructed using pivot table functions in Microsoft Excel. The overall accuracy, producer's accuracy, user's accuracy, and Kappa coefficient were then calculated as provided in the methodology of Congalton and Green [40]. The accuracy assessment results for the land use/land cover maps derived from the selected Landsat scenes acquired in May of 2010, 2011, 2013, 2016, and 2018 are presented and discussed in Section 3. The error matrix is a standard and widely used tool for evaluating classification performance. However, some level of classification error is unavoidable. These errors occur because not all classified pixels correspond perfectly to their actual land cover classes. This can happen due to mixed pixels and the spectral similarities between different land cover types [41].

2.7 Retrieving the Land Surface Temperature (LST)

Several methods have been proposed in the literature for retrieving land surface temperature (LST) from thermal infrared satellite data. One of the earliest approaches is the generalized single-channel method, which estimates LST using a single thermal band [19]. This method has been extended to generalized two-channel (or split-window) algorithms that exploit the differential atmospheric absorption between two adjacent thermal bands [42]. For Landsat-8, the split-window method uses TIRS bands 10 (10.60–11.19 µm) and 11 (11.50–12.51 µm) to calculate LST. Various split-window equations have been proposed and validated for different sensors and atmospheric environments [43][44][45][46] and [47]. Other algorithms specifically account for the effects of water vapor in the atmosphere. The split-window covariance–variance ratio (SWCVR) method allows the total atmospheric water vapor (W) to be estimated from satellite data [46]. Based on this method, the SWCVR approach was adapted in [48] for the retrieval of column water vapor (CWV) from Landsat-8 TIRS data, assuming that the atmospheric conditions for a set of neighboring pixels can be treated as uniform. The CWV is estimated from the transmittance ratio of the top-of-atmosphere (TOA) brightness temperatures of the two TIRS bands.

For Landsat-5 thermal calibration, the NDVI threshold method was applied for land surface emissivity correction [16]. The Normalized Difference Vegetation Index (NDVI) is a widely recognized index in vegetation science that indicates the amount of vegetation present, the density of that vegetation, and its condition. NDVI is defined as a ratio based on reflectance values in the near-infrared (NIR) and red (RED) portions of the electromagnetic

ISSN: 1686-6576 (Printed) | ISSN 2673-0014 (Online) |

spectrum [49]. It is mathematically expressed as the difference between the NIR and RED bands divided by their sum [50]. In this analysis, NDVI was calculated using the atmospherically corrected surface reflectance values of the red (Surface reflectance of visible red band) and near-infrared bands (Surface reflectance of near-infrared bands) derived from Landsat imagery. NDVI values range from −1 to +1. Negative or nearly zero values of NDVI relate to water bodies, while positive values relate to soil and vegetation. NDVI values between approximately 0.2 and 0.6 indicate sparse to moderate vegetation cover, whereas higher values approaching 0.8 are associated with dense and healthy vegetation. The calculation of NDVI (Equation 1) is essential for estimating the proportion of vegetation for a given pixel (P_v) or sometimes called the Fractional Vegetation Cover (FVC) which is highly related to NDVI and emissivity (ε) [51]. NDVI was calculated from the reflectance values of the visible red and near-infrared bands using the established formulation [15] as in Equation 1:

$$NDVI = \frac{NIR - RED}{NIR + RED}$$

Equation 1

Where:
$NDVI$ = Normalized Difference Vegetation Index
NIR = Near-infrared bands
RED = Visible band red (for Landsat-8 Band 4)

The proportion of vegetation for a given pixel (P_v) was calculated using the NDVI threshold method [51] as in Equation 2:

$$P_v = \left(\frac{NDVI - NDVI_{\min}}{NDVI_{\max} - NDVI_{\min}} \right)^2$$

Equation 2

Where:
$NDVI_{min}$ = Minimum NDVI value
$NDVI_{max}$ = Maximum NDVI value

Surface emissivity was estimated from NDVI by considering different vegetation-cover conditions according to the established approach [20] and [52]: (a) NDVI < 0.2 in this case, the pixel is considered as bare soil and the emissivity is obtained from reflectivity values in the red region; (b) NDVI>0.5 pixels with NDVI values higher than 0.5 are considered as fully vegetated, and then a constant value for the emissivity is assumed, typically of 0.99; and (c) 0.2 ≤ NDVI ≤ 0.5 in this case, which is our case, the pixel is composed by a mixture of bare soil and vegetation which is a common case, and the land surface emissivity (ε) is calculated according to Equation 3:

$$\varepsilon = \varepsilon_v P_v + \varepsilon_s (1-P_v)$$

Equation 3

Where ε_s and ε_v are soil emissivity, and vegetative emissivity of the corresponding bands. Following the approach presented in [20], the final expression for emissivity is given by Equation 4:

$$\varepsilon = 0.004P_v + 0.986$$

Equation 4

Although emissivity was calculated on a pixel-by-pixel basis using the NDVI-threshold method rather than assigned by land-cover class, the values generally fall within the ranges reported in Table 5. Vegetated surfaces exhibit the highest emissivity, whereas barren soils and built-up surfaces typically have lower emissivity values.

Table 5: Typical land surface emissivity ranges for the major land-cover classes [20] and [52]

Land-cover class	Typical emissivity range
Urban	0.94–0.97
Vegetation	0.98–0.99
Rangeland	0.95–0.98
Barren land	0.92–0.96
Water	0.99

Satellite TIR sensors measure top of atmosphere (TOA) radiances, from which brightness temperatures (also known as blackbody temperatures) can be derived using Planck's law [16] and [53] as in Equation 5:

$$\rho = h\frac{C}{\sigma}$$

Equation 5

Where:
ρ = second radiation constant (1.438×10^{-2} m·K)
σ = Boltzmann constant (1.38×10^{-23} J/K)
h = Planck's constant (6.626×10^{-34} J s)
C = velocity of light (2.998×10^{8} m/s)

The emissivity-corrected land surface temperature (LST) was then estimated using the single-channel algorithm based on Planck's radiation law. For Landsat-5 TM, LST was retrieved from the at-sensor brightness temperature after emissivity correction as in Equation 6:

$$T_s = \frac{BT}{1 + \left(\frac{L_\lambda BT}{\rho}\right)\ln(\varepsilon)} - 237.15$$

Equation 6

Where:

T_s = Land syrface temperature (°C)

BT = At-sensor brightness temperature (K).

L_λ = Effective wavelength of the Landsat-5 TM thermal band (11.45 μm) used in the single-channel LST retrieval.

The L_λ is not required for Landsat-8 because LST was retrieved using the ENVI®5.5 thermal correction module implementing the NEM/TES algorithm.

Equation 6 computes the emissivity-corrected land surface temperature using brightness temperature expressed in Kelvin. The resulting LST is converted to degrees Celsius by subtracting 273.15, as indicated in the final term of the equation.

Several methods have been proposed to estimate land surface emissivity, including the Alpha-Derived Emissivity (ADE), Emissivity Bounds Method (EBM), Graybody Emissivity Method (GEM), and Normalized Emissivity Method (NEM) [54]. These emissive correction approaches are designed to account for variations in surface radiative properties, particularly in areas characterized by mixed pixels, thereby improving the accuracy of land surface temperature (LST) retrieval. The surface emissions derived from the NDVI threshold method were used to correct LST estimates for Landsat-5 imagery. For Landsat-8 data, the Environment for Visualizing Images (ENVI®5.5) software was employed to estimate LST using the NEM model through its thermal correction tool. This approach represents a methodological advancement in emissivity correction, as it enables simultaneous retrieval of emissivity and surface temperature.

The use of different emissivity estimation methods was influenced by the types of thermal sensors used in each Landsat mission. Landsat-5 TM features only one thermal infrared band, which limits the ability to use temperature-emissivity separation algorithms like the Normalized Emissivity Method (NEM). As a result, the NDVI-threshold method was utilized for estimating land surface emissivity with Landsat-5 imagery. In contrast, Landsat-8 includes two thermal infrared bands (TIRS Bands 10 and 11), which allows the ENVI®5.5 thermal correction module to apply the NEM/TES algorithm for the simultaneous retrieval of surface emissivity and land surface temperature. In addition, radiometric calibration updates and stray-light correction have substantially improved the thermal accuracy of Landsat-8 TIRS, enhancing the reliability of land surface temperature retrievals [55]. Although both methods are widely accepted and validated for their respective sensors, minor uncertainties may arise when comparing LST values derived from different sensors. To minimize these effects, all Landsat scenes were acquired during the same season (May) under comparable environmental conditions, and consistent preprocessing and analysis procedures were applied wherever possible. Consequently, the observed spatial and temporal temperature patterns are considered representative of actual land surface conditions, while acknowledging that some uncertainty associated with cross-sensor comparisons cannot be completely eliminated.

The temperature/emissivity separation (TES) algorithm based on the NEM model has been shown to retrieve LST from Landsat 8 thermal bands with an RMSE of approximately 0.7 K [51], demonstrating higher accuracy than the single-channel (RMSE ≈ 1.7 K [19]) and split-window (RMSE ≈ 1.0 K [56]) approaches. The main advantage of the NEM method is that it has been shown to provide accurate emissivity estimates, leading to high-quality LST retrievals from satellite thermal infrared measurements [51]. In this analysis, the NEM algorithm applied in ENVI®5.5 was used to generate emissivity-corrected LST images, which were subsequently converted to degrees Celsius for analysis. The selection of the NEM algorithm is important for this arid setting because of its enhanced ability to decouple temperature and emissivity in regions of mixed pixel density and sparse vegetation (NDVI < 0.2). The NEM algorithm is particularly suitable for reducing temperature–emissivity uncertainty over hot, sparsely vegetated surfaces. Accordingly, the high LST values observed over exposed rangeland are physically plausible, although some uncertainty associated with emissivity estimation and thermal retrieval remains. These characteristics are expected to improve the reliability of the retrieved LST and support the interpretation of the observed NDVI–LST and UHI patterns.

Surface emissivity plays an important role in LST retrieval because errors in emissivity propagate directly into temperature estimates. In general, vegetated surfaces exhibit relatively high emissivity values, whereas barren soils and built-up materials have lower emissivity. Because emissivity was estimated from NDVI (Landsat-5) or retrieved through the NEM/TES algorithm (Landsat-8), spatial variations in vegetation cover were incorporated into the LST retrieval process. Nevertheless, minor uncertainties in emissivity estimation may introduce small errors in the calculated LST, particularly over

ISSN: 1686-6576 (Printed) | ISSN 2673-0014 (Online) | © Geoinformatics International

sparsely vegetated and exposed soil surfaces. Independent validation using ground-based thermal measurements is generally recommended to quantify the accuracy and uncertainty of satellite-derived LST, particularly where emissivity varies substantially among land-cover types [57].

2.8 Estimation of intensity of Urban Heat Island (UHI)

The UHI effect was quantified using an index that represents normalized temperature variations across different land-cover types [58] as in Equation 7:

$$UHI = \frac{T - T_{mean}}{T_{mean}}$$

Equation 7

Where:

UHI = Urban heat island index

T = Final land surface temperature map (°C)

T_{mean} = Mean temperature value (°C)

Satellite-derived land surface temperature has been widely used to characterize the spatial distribution and intensity of surface urban heat islands and to investigate their relationship with land use/land cover change [59].

The UHI index used in the present work is a normalized land surface temperature (LST)-based indicator that characterizes the relative spatial distribution of daytime surface thermal conditions within the study area. It does not represent the classical atmospheric urban heat island defined by urban-rural air temperature differences. Instead, it provides a relative measure of surface thermal intensity derived from remotely sensed LST and is intended to identify spatial variations in daytime surface heating associated with different land-cover types.

The calculated UHI values were classified in ArcGIS using consistent class intervals to facilitate visualization and comparison among the selected study years. These intervals were used for map presentation only and should not be interpreted as physically defined temperature thresholds. Negative UHI values represent areas with LST below the study-area mean, whereas positive values indicate progressively warmer surfaces relative to the mean. Urban heat island (UHI) intensity in an urban area can be divided into three classes in terms of surface materials, namely low (vegetation, water), medium (built-up area with vegetation buffer), and high (dense built-up area and exposed soils). These classes can be related to variations in surface energy balance, evapotranspiration and heat storage. The UHI intensity was calculated using satellite derived LST for the whole city. The UHI intensity index was classified into four classes (0, 0.1, 0.2) in order to better reflect the local variability of the surface materials. The first class (UHI = 0) corresponds to areas with no UHI effect, such as water bodies and densely vegetated areas. The second class (UHI = 0 – 0.1) corresponds to areas with weak UHI effect, such as sparsely vegetated areas. The third class (UHI = 0.1 – 0.2) corresponds to moderate UHI effect and encompasses most built-up urban areas. The last class (UHI = 0.2) corresponds to strong UHI effect and is mainly composed of exposed soils and rangelands. This classification allows for an accurate spatial analysis of UHI intensity and comparison between urban areas, vegetated areas and barren areas. By relating each class of UHI intensity to the corresponding land use and land cover types, this approach highlights the influence of land-cover composition on surface temperature patterns, particularly in arid environments where exposed soils may exhibit higher temperatures than built-up areas.

3. Results and Discussion

3.1 Classification Maps

Land use/land cover (LULC) classification maps generated using the maximum likelihood classifier (MLC) were produced for Sunland Park for the years 2010, 2011, 2013, 2016, and 2018 (Figure 4). Figure 5 presents a histogram for the distributed areas of each land cover class, including urban, vegetation, rangeland, water, and barren land. The urban territory grew from 7.5 square kilometers during 2010 to 12.2 square kilometers during 2018 while rangeland territories shrunk from 17.8 square kilometers to 12.3 square kilometers between 2010 and 2018. The data indicate that urban development took most of its land from rangeland areas. Water body classes were consistently and accurately assigned across all years. The water body classes corresponded to the Rio Grande, which is the primary surface water feature of the study area.

ISSN: 1686-6576 (Printed) | ISSN 2673-0014 (Online) | © Geoinformatics International

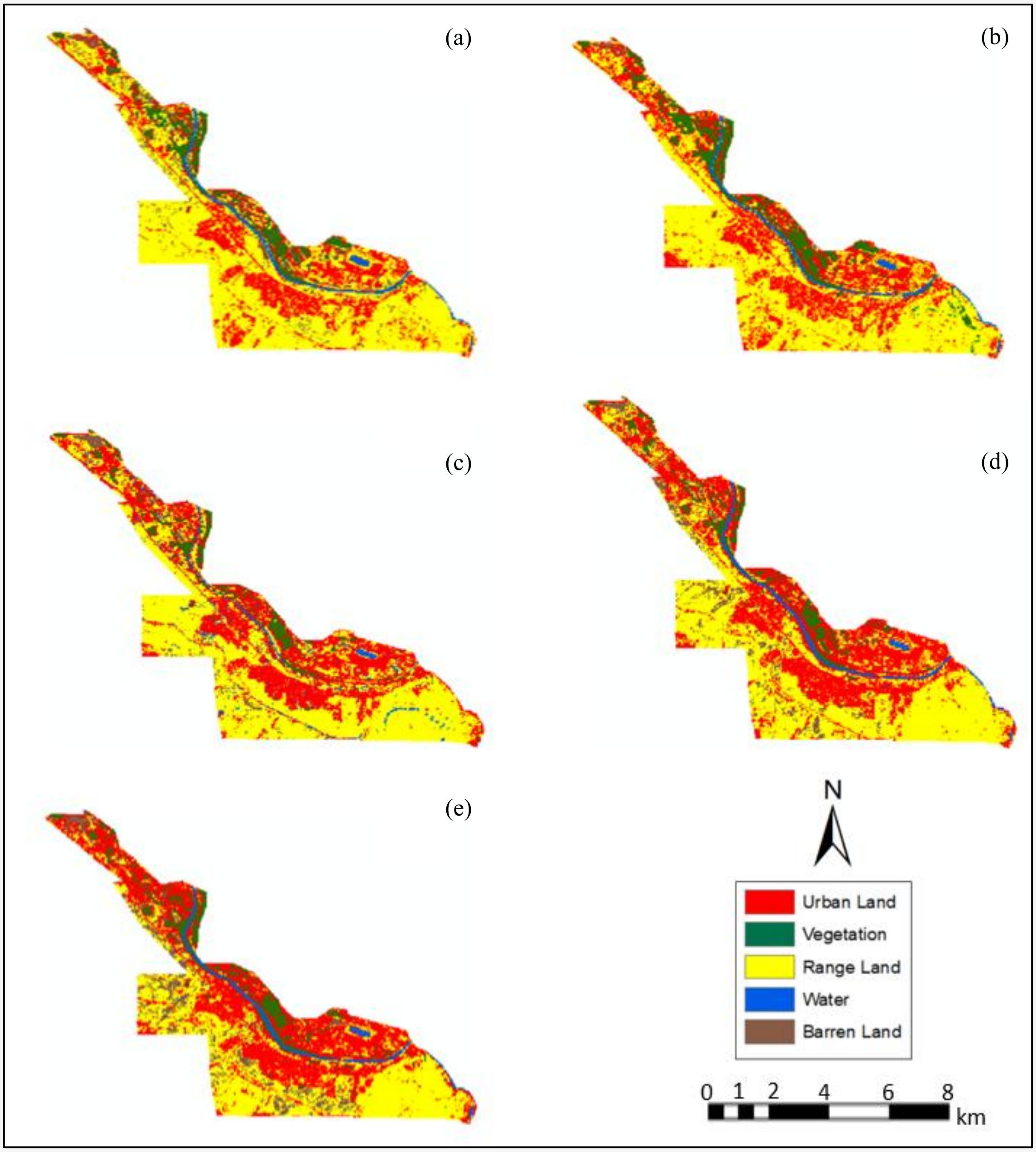

Figure 4: Land cover: (a) 2010, (b) 2011, (c) 2013, (d) 2016, and (e) 2018

The area extent of barren land and agricultural land showed moderate variability from year to year, with increases in cultivated area generally occurring simultaneously with decreases in barren land that suggest land use conversions between these two classes. The increase of 0.2 km² in barren land area for 2016 and 0.5 km² for 2018 may represent classification errors or false positives that interpreted barren land as sparse vegetation areas. However, these minor fluctuations did not alter the overall pattern of land cover change that was identified across the study period: the persistent expansion of urban area. Additional area calculations for each class reveal that urban growth and development, especially the expansion of buildings and residential areas, steadily increased from 2010 to 2018, with the greatest rates of expansion occurring in the southwestern part of Sunland Park.

ISSN: 1686-6576 (Printed) | ISSN 2673-0014 (Online) | © Geoinformatics International

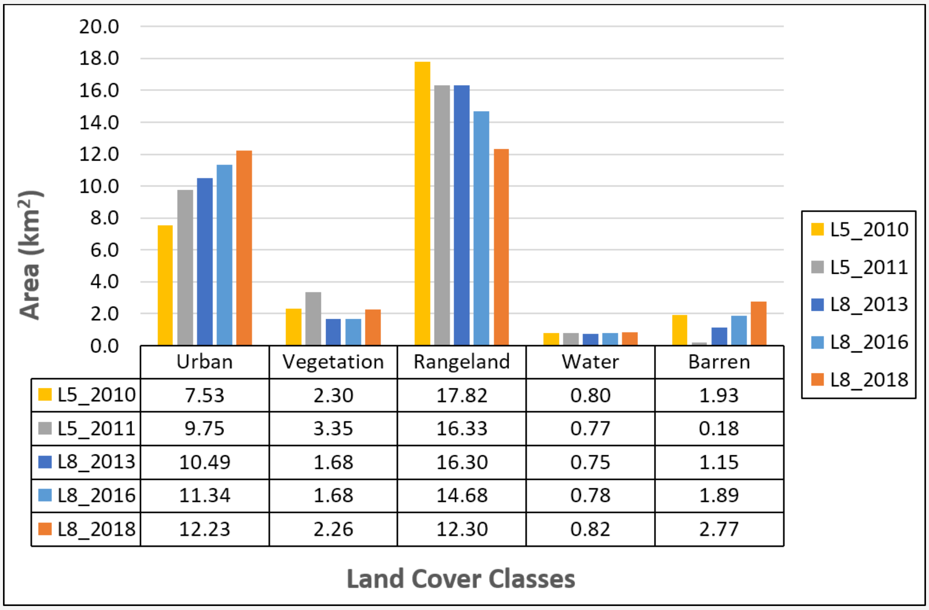

Figure 5: Land cover change histogram represents the areas for each class for the years 2010, 2011, 2013, 2016, and 2018

Table 6: Changes in urban land and rangeland between 2010 and 2018

Land Cover Class	2010 (km²)	2018 (km²)	Absolute Change (km²)	Relative Change (%)
Urban	7.53	12.23	+4.70	+62.4
Rangeland	17.82	12.30	−5.52	−31.0

3.2 Change Detection Results

Remote sensing–based change detection showed that there were large-scale changes in land cover in Sunland Park over the period of 2010 to 2018, with the highest rates of change for urban and rangeland areas. To provide a clearer interpretation of land-cover changes between 2010 and 2018, Table 6 summarizes the changes in urban land and rangeland between 2010 and 2018, including the corresponding land-cover area, absolute area change (km²), and relative percentage change with respect to the 2010 area. Reporting both measures provides a clearer assessment of the magnitude and direction of the observed land-cover changes. As shown in Figure 6, rangeland exhibit the highest rate of loss, at about –18.1%, and urban areas present the highest rate of gain, at about +15.5%. The most common change in land cover was the transition from rangeland to urban areas, such as due to urbanization.

Between 2010 and 2018, urban land increased from 7.53 km² to 12.23 km², representing an absolute increase of 4.70 km² (62.4% relative to its 2010 area). In contrast, rangeland decreased from 17.82 km² to 12.30 km², corresponding to an absolute loss of 5.52 km² (31.0% relative to its 2010 area). Change detection analysis also indicated a slight increase in water area of approximately 0.1% between 2010 and 2018, corresponding mainly to the Rio Grande River (Figure 6). For comparison, the U.S. Department of Agriculture (USDA) Cropland Data Layer (CDL) maps for the same period show an increase in water area from approximately 0.058 km² to 1.0 km², representing an increase of about 0.3%. The discrepancy between the two estimates is considered acceptable and can be attributed to differences in classification methods, spatial resolution, and data sources. Consequently, the 0.1% increase in water area derived from the Landsat-based classification is considered reasonable when compared with the USDA CDL results.

3.3 Accuracy Assessments

The visual accuracy assessment using Google Earth Pro images for the years 2010, 2013, and 2018 clearly demonstrated the progress in urban land for selected various locations in the city (Figure 7). Meanwhile, the highest overall accuracies and Kappa coefficients, 87.3% and 78% respectively, were determined for the year 2010 (Table 7). The accuracy assessment for remote sensing data can be accepted if it is greater than 70 % [60]. Table 7 presents all calculated accuracies (error matrix) for each classified map.

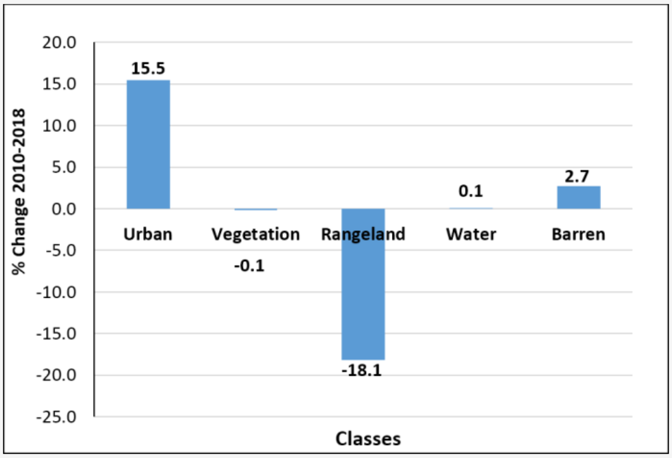

Figure 6: Land cover post-classification change detection percentage for each class was established between 2010 and 2018 (Derived using Landsat data)

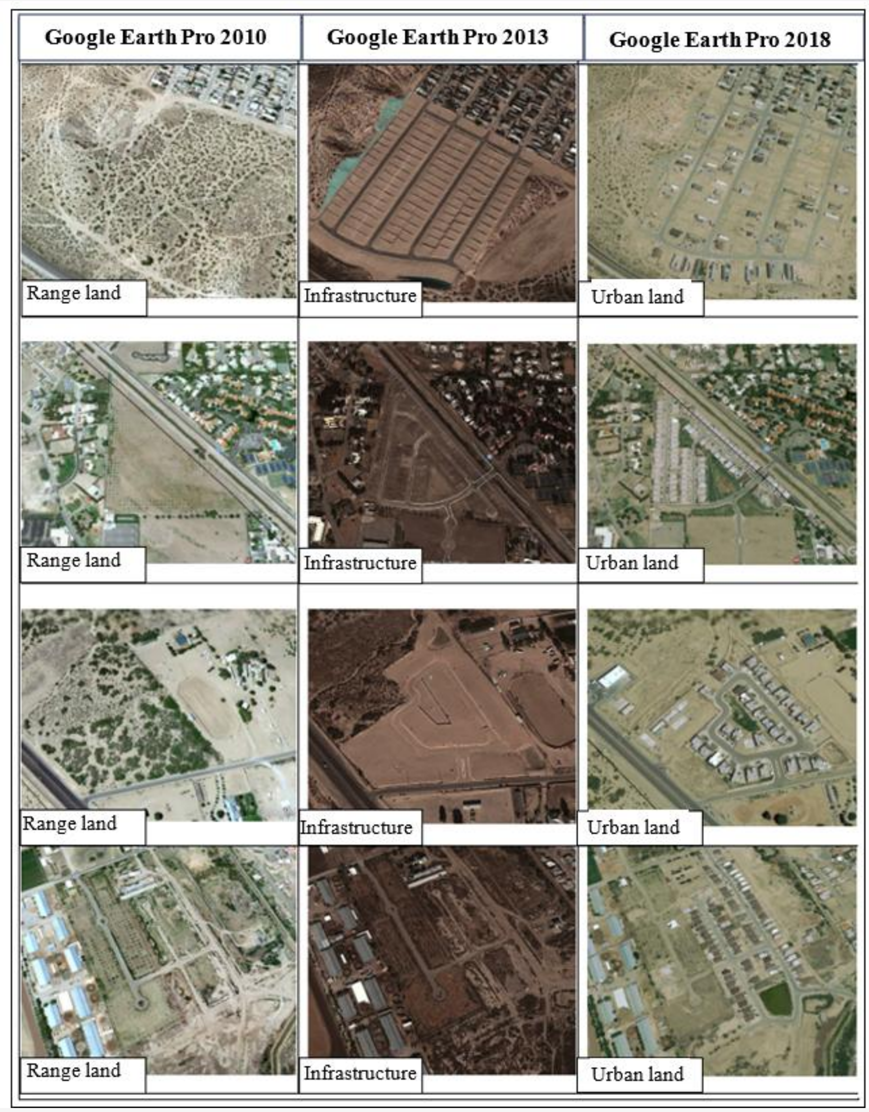

Figure 7: Representative Google Earth Pro images used for visual interpretation and validation of the LULC classes, selected from locations across the study area

ISSN: 1686-6576 (Printed) | ISSN 2673-0014 (Online) | © Geoinformatics International

Table 7: Confusion matrix (error) accuracy assessments for the classified images for the selected Landsat scenes acquired in May of 2010, 2011, 2013, 2016, and 2018 (continue next page)

Classified Map (2010)	Ground Truth (Google Map 2010)					
	Urban Land	**Vegetation**	**Range Land**	**Water**	**Barren Land**	**Total**
Urban Land	60	1	8	1	4	**74**
Vegetation	1	17	3	1	1	**23**
Range Land	6	0	168	0	3	**177**
Water	0	1	0	8	0	**9**
Barren Land	0	0	8	0	9	**17**
Total	**67**	**19**	**187**	**10**	**17**	**300**
Producer accuracy (%)	90	89	90	80	53	
User accuracy (%)	81	74	95	89	53	
Overall accuracy (%)	**87.3**					
Kappa Coefficient (%)	**78**					

Classified Map (2011)	Ground Truth (Google Map 2011)					
	Urban Land	**Vegetation**	**Range Land**	**Water**	**Barren Land**	**Total**
Urban Land	66	0	19	0	8	**93**
Vegetation	0	38	1	0	0	**39**
Range Land	0	0	143	0	0	**143**
Water	7	0	2	8	4	**21**
Barren Land	0	0	0	1	3	**4**
Total	**73**	**38**	**165**	**9**	**13**	**300**
Producer accuracy (%)	90	100	87	89	23	
User accuracy (%)	71	97	100	38	75	
Overall accuracy (%)	**86.0**					
Kappa Coefficient (%)	**78**					

Classified Map (2013)	Ground Truth (Google Map 2013)					
	Urban Land	**Vegetation**	**Range Land**	**Water**	**Barren Land**	**Total**
Urban Land	75	1	20	0	1	**97**
Vegetation	2	13	2	0	1	**18**
Range Land	5	0	161	2	0	**168**
Water	1	0	2	2	0	**5**
Barren Land	2	0	4	0	6	**12**
Total	**85**	**14**	**189**	**4**	**8**	**300**
Producer accuracy (%)	88	93	85	50	75	
User accuracy (%)	77	72	96	40	50	
Overall accuracy (%)	**85.7**					
Kappa Coefficient (%)	**74**					

Table 7: Confusion matrix (error) accuracy assessments for the classified images for the selected Landsat scenes acquired in May of 2010, 2011, 2013, 2016, and 2018 (continue from previous page)

Classified Map (2016)	Ground Truth (Google Map 2016)						
		Urban Land	**Vegetation**	**Range Land**	**Water**	**Barren Land**	**Total**
	Urban Land	76	4	15	1	6	**102**
	Vegetation	3	11	0	0	0	**14**
	Range Land	0	1	157	1	0	**159**
	Water	0	0	0	6	0	**6**
	Barren Land	1	0	10	0	8	**19**
	Total	**80**	**16**	**182**	**8**	**14**	**300**
	Producer accuracy (%)	95	69	86	75	57	
	User accuracy (%)	75	79	99	100	42	
	Overall accuracy (%)	**86.0**					
	Kappa Coefficient (%)	**76**					

Classified Map (2018)	Ground Truth (Google Map 2018)						
		Urban Land	**Vegetation**	**Range Land**	**Water**	**Barren Land**	**Total**
	Urban Land	94	3	18	0	5	**120**
	Vegetation	2	21	2	0	0	**25**
	Range Land	5	0	123	0	1	**129**
	Water	0	0	0	10	0	**10**
	Barren Land	0	0	9	0	7	**16**
	Total	**101**	**24**	**152**	**10**	**13**	**300**
	Producer accuracy (%)	93	88	81	100	54	
	User accuracy (%)	78	84	95	100	44	
	Overall accuracy (%)	**85.0**					
	Kappa Coefficient (%)	**76**					

The overall classification accuracy exceeded 85% for all study years, indicating reliable land-cover classification performance. Urban and vegetation classes generally achieved high producer's and user's accuracies, reflecting their relatively distinct spectral characteristics. In contrast, rangeland and barren land exhibited comparatively lower accuracies because these classes often share similar spectral responses under arid environmental conditions. Water also showed lower accuracy in some years because of its limited spatial extent and the relatively small number of reference samples. Nevertheless, the relatively high producer's and user's accuracies for the major land-cover classes, together with the consistency of the observed spatial temperature patterns across all study years, indicate that the remaining classification uncertainty is unlikely to affect the main conclusions regarding the influence of land cover on land surface temperature and surface urban heat island patterns [61].

3.4 Spatial Distribution of LST and NDVI

Normalized Difference Vegetation Index (NDVI) maps were generated for the same study years as the LST maps. For Landsat-5, NDVI was additionally used in emissivity estimation through the NDVI-threshold method, whereas for Landsat-8 it was used independently for interpretation of the NDVI–LST relationship. Previous research used NDVI to track how urban growth affects LST through temperature increases but most studies made the incorrect assumption that urbanization leads to a straight upward trend in land surface temperature. The study investigated NDVI and LST relationships through a polynomial model which defined their connection. The data indicates that LST values decrease when NDVI values achieve their minimum values. The NDVI values in these areas reached their highest points because they contained mostly vegetation which produced lower surface temperatures. The spatial connection between these elements becomes evident through Figure 8 which illustrate green areas with high NDVI values that match blue areas with

ISSN: 1686-6576 (Printed) | ISSN 2673-0014 (Online) |

low LST values. Moreover, the qualitative visual interpretation of the LST and NDVI maps confirmed the expected inverse relationship between vegetation cover and land surface temperature. Areas with high NDVI values, representing dense vegetation, generally exhibited lower LST due to the combined effects of shading and evapotranspiration, which dissipate a portion of the absorbed solar energy as latent heat, consistent with previous findings for irrigated vegetation in arid environments [62]. Water bodies, characterized by NDVI values close to or below zero, also exhibited relatively low LST because of their high heat capacity and evaporative cooling. In contrast, built-up areas and exposed soils were associated with low NDVI and higher LST, reflecting limited vegetation cover, reduced soil moisture, and a greater proportion of absorbed energy converted to sensible heat. Similar thermal differences among land-cover classes have been widely reported in previous urban remote sensing studies [16].

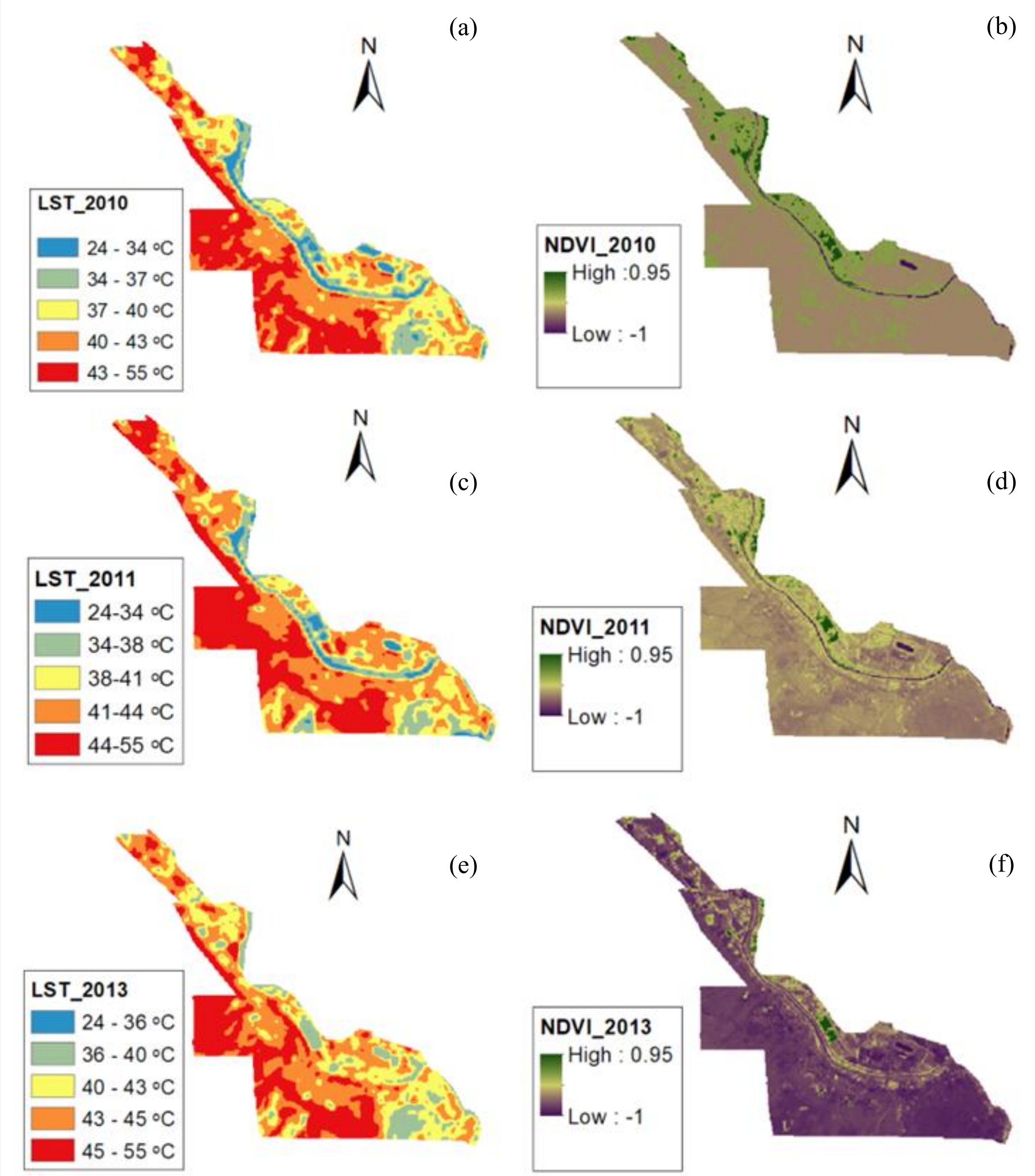

Figure 8: Land surface temperature and NDVI: (a) 2010 LST, (b) 2010 NDVI, (c) 2011 LST, (d) 2011 NDVI, (e) 2013 LST, (f) 2013 NDVI, (g) 2016 LST, (h) 2016 NDVI, (i) 2018 LST, and (j) 2018 NDVI (Continue next page)

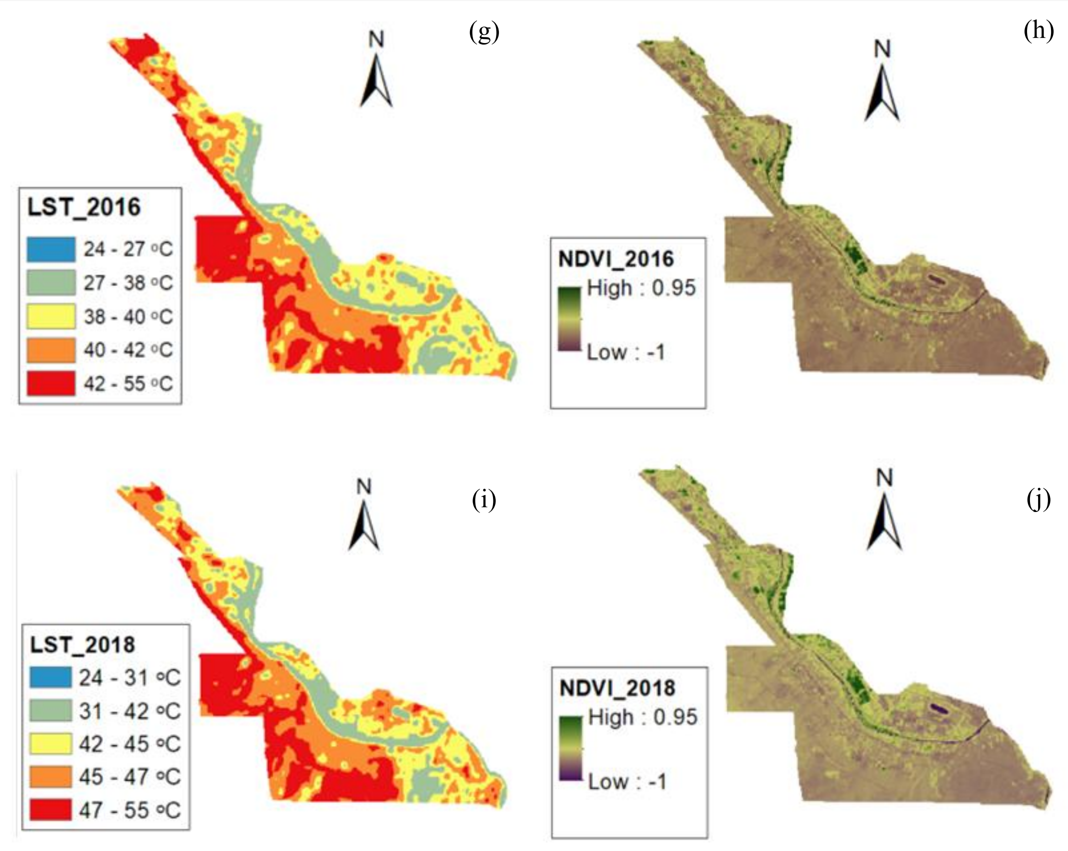

Figure 8: Land surface temperature and NDVI: (a) 2010 LST, (b) 2010 NDVI, (c) 2011 LST, (d) 2011 NDVI, (e) 2013 LST, (f) 2013 NDVI, (g) 2016 LST, (h) 2016 NDVI, (i) 2018 LST, and (j) 2018 NDVI (Continue from page)

Although the LST and NDVI maps clearly illustrate the spatial distribution of surface temperature, quantitative statistics are necessary to objectively compare the thermal characteristics of the different land-cover classes. Therefore, descriptive statistics, including the mean, median, minimum, maximum, and standard deviation of LST, were calculated for each land-cover class and each study year (Table 8). The results presented in Table 8 quantitatively confirm the spatial patterns observed in the LST maps. Across the five study years, rangeland and barren land consistently exhibited the highest daytime LST among the terrestrial land-cover classes, whereas vegetation and water remained the coolest surfaces. In most years, rangeland showed the highest mean LST, while barren land was slightly warmer than rangeland in 2016. Urban areas generally exhibited lower daytime LST than both rangeland and barren land, indicating that exposed dry surfaces can attain higher temperatures than built-up areas under arid climatic conditions. These quantitative results support the visual interpretation of the LST maps and strengthen the conclusion that land-cover composition exerts a strong influence on daytime thermal behavior in the study area.

The highest land surface temperatures (LST) were primarily observed in the southwestern portion of the study area, where both urban areas and extensive exposed barren soils are located (Figure 8, left). The LST maps consistently show that barren land and sun-exposed sandy soils exhibited higher daytime surface temperatures than most urban areas. This behavior is attributed to the limited vegetation cover and low soil moisture of exposed surfaces, which restrict evaporative cooling and increase the proportion of absorbed solar energy converted into sensible heat. In contrast, some urban areas exhibited comparatively lower LST, likely because of the presence of irrigated vegetation, shading, and differences in surface characteristics. The consistent spatial patterns observed across all selected May Landsat scenes support the interpretation that land-cover characteristics play an important role in controlling the daytime thermal environment in this arid region. Shade from both buildings and trees planted in urban areas has helped to decrease the

ISSN: 1686-6576 (Printed) | ISSN 2673-0014 (Online) | © Geoinformatics International

amount of solar radiation absorption [14], which in turn has reduced LST and created pleasant and calm weather. The water class (Rio Grande River) has a lower NDVI value than the barren and urban areas (NDVI≤ 0) as well as a lower LST value across the study years. Table 9 presents the general statistical measures (maximum, minimum, mean, and standard deviation) derived from the LST and NDVI maps generated from the selected Landsat scenes acquired in May of 2010, 2011, 2013, 2016, and 2018. Section 3.5 provides a detailed assessment of the relationship between LST and NDVI.

Table 8: Class-wise descriptive statistics of land surface temperature (°C) for each land-cover class during the selected images from 2010–2018

Year	Land-cover class	Mean (°C)	Median (°C)	Min (°C)	Max (°C)	Std. (°C)
2010	Urban	40.12	40.86	30.07	48.38	2.44
	Vegetation	36.46	36.68	25.53	45.95	3.21
	Rangeland	42.03	42.82	31.82	48.45	2.87
	Water	32.80	32.98	24.66	42.07	2.74
	Barren land	41.34	41.66	30.17	49.50	3.01
2011	Urban	41.81	42.59	28.35	49.57	2.51
	Vegetation	38.16	38.78	26.25	47.03	3.63
	Rangeland	43.51	44.08	28.77	49.57	3.31
	Water	34.33	34.46	24.11	42.59	2.72
	Barren land	42.82	42.96	32.05	49.57	2.69
2013	Urban	45.80	46.06	32.81	51.75	1.81
	Vegetation	44.38	44.89	31.45	52.51	3.32
	Rangeland	46.67	47.11	36.15	52.05	2.53
	Water	45.80	46.31	31.72	51.41	2.78
	Barren land	46.46	46.68	33.90	51.66	2.07
2016	Urban	42.18	42.61	30.73	47.64	2.26
	Vegetation	40.20	40.70	31.72	46.37	2.94
	Rangeland	43.42	43.73	31.35	48.06	2.39
	Water	38.03	38.31	29.76	42.13	2.35
	Barren land	44.45	44.84	32.58	48.12	2.11
2018	Urban	47.37	47.80	38.11	51.86	1.90
	Vegetation	45.06	45.62	35.29	55.20	3.00
	Rangeland	48.93	49.65	40.54	54.80	2.55
	Water	40.63	40.84	33.58	46.61	2.22
	Barren land	48.58	48.76	37.85	55.06	2.22

Table 9: Some statistical values for LST and NDVI derived from Landsat data for the years 2010, 2011, 2013, 2016, and 2018 using ENVI®5.5

	LST ($^{\circ}C$)				NDVI (-1 to 1)			
Year	**Max.**	**Min.**	**Mean**	**Std.**	**Max.**	**Min.**	**Mean**	**Std.**
Landsat-5 2010	50	24	41	3.50	0.81	-0.49	0.18	0.01
Landsat-5 2011	51	24	43	3.70	0.90	-0.63	0.15	0.09
Landsat-8 2013	53	31	46	2.77	0.95	-0.23	0.16	0.11
Landsat-8 2016	49	30	42	2.57	0.94	-0.49	0.19	0.12
Landsat-8 2018	55	34	47	3.04	0.93	-1.00	0.18	0.13

3.5 Analysis of LST and NDVI Maps

To improve understanding of the LST and NDVI pattern, the LST and NDVI images of Sunland Park city are displayed simultaneously with the aid of ENVI®5.5 software. The LST-NDVI polynomial relationships were analyzed by extracting the ground pixel's values from each NDVI map for selected Landsat scenes acquired in May of 2010, 2011, 2013, 2016, and 2018 along with the corresponding LST values at the exact location. The horizontal profile for both the LST and NDVI maps was generated using ENVI®5.5; then the values were used to perform the regressions between them.

Due to the large number of pixel values available in both the LST and NDVI maps, the NDVI–LST relationship was evaluated by extracting corresponding NDVI and LST values along a horizontal profile generated in ENVI®5.5. The

ISSN: 1686-6576 (Printed) | ISSN 2673-0014 (Online) |

profile was positioned across the central portion of the study area to intersect representative land-cover types. A total of 160 corresponding sample values were extracted and used to develop polynomial regression. NDVI values less than zero, representing water bodies, were excluded from the analysis because water surfaces typically exhibit low or negative NDVI values together with relatively low land surface temperatures. In contrast, barren land surfaces also exhibit low NDVI values but generally have substantially higher land surface temperatures. Including water pixels in the regression would therefore weaken the NDVI–LST relationship and potentially bias the regression results. This profile-based approach was adopted to examine the spatial relationship between NDVI and LST along a representative transect. Excluding water pixels improves the representation of the relationship between vegetation cover and land surface temperature across the terrestrial land-cover classes [63]. The statistical performance of the second-order polynomial regression models developed between NDVI and LST for each study year is summarized in Table 10. All regression models were statistically significant ($p < 0.001$), indicating a significant nonlinear relationship between vegetation cover and land surface temperature. The 95% confidence intervals of the regression coefficients did not include zero, confirming the statistical significance of the fitted polynomial terms. Furthermore, the relatively low residual standard errors and the absence of pronounced systematic patterns in the residuals indicate that the fitted polynomial models provided a reasonable representation of the nonlinear relationship between NDVI and LST within the sampled data. The corresponding second-order polynomial regression curves and their fitted equations for the years 2010, 2011, 2013, 2016, and 2018 are presented in Figure 9.

From the LST-NDVI relationships presented above for the selected Landsat scenes acquired in May of 2010, 2011, 2013, 2016, and 2018, the land surface temperatures were observed to be high values for the corresponding NDVI values that were less than 0.2. The aggregated points on the top left side for each curve illustrate that the majority of areas at Sunland Park city are barren lands. As shown in Figure 9, the NDVI values can be broadly divided into three ranges. The first range (NDVI = 0–0.2) is associated with relatively high LST values and represents predominantly barren land and urban surfaces. The second range (NDVI = 0.2–0.4) corresponds to moderate LST values. The third range (NDVI > 0.4) is associated with comparatively lower LST values and represents vegetated areas. The relatively small number of observations within the third range reflects the limited extent of cultivated and densely vegetated land in Sunland Park. Overall, the results demonstrate a clear inverse relationship between NDVI and LST.

It should be noted that the NDVI–LST regression was based on samples extracted along a horizontal profile rather than a stratified random sampling design. Consequently, the regression results should be interpreted as an assessment of the spatial relationship between NDVI and LST along a representative transect rather than a class-wise statistical analysis. Future studies may benefit from applying stratified random sampling across all land-cover classes and incorporating additional statistical diagnostics. In conclusion, expansion of the cultivated or vegetation area by planting trees among urban developments will cause corresponding higher rates of evapotranspiration and will control the latent and sensible heat exchange between the land surface and atmosphere which results in reduction in land surface temperature.

3.6 Spatial Distribution of UHI Over the City

The Urban Heat Island (UHI) index was classified into four distinct categories to represent spatial variations in surface thermal intensity across Sunland Park (Figure 10). These categories provide a detailed depiction of the relationship between land cover types and surface temperature patterns.

Table 10: Statistical diagnostics of the second-order polynomial regression models between NDVI and LST

Year	Sample Size (n)	R^2	Residual Standard Error	F-statistic	p-value
2010	160	0.7	1.81	147.8	< 0.001
2011	160	0.6	2.18	101.0	< 0.001
2013	160	0.8	1.74	314.5	< 0.001
2016	160	0.7	1.42	161.0	< 0.001
2018	160	0.7	1.51	183.7	< 0.001

ISSN: 1686-6576 (Printed) | ISSN 2673-0014 (Online) | © Geoinformatics International

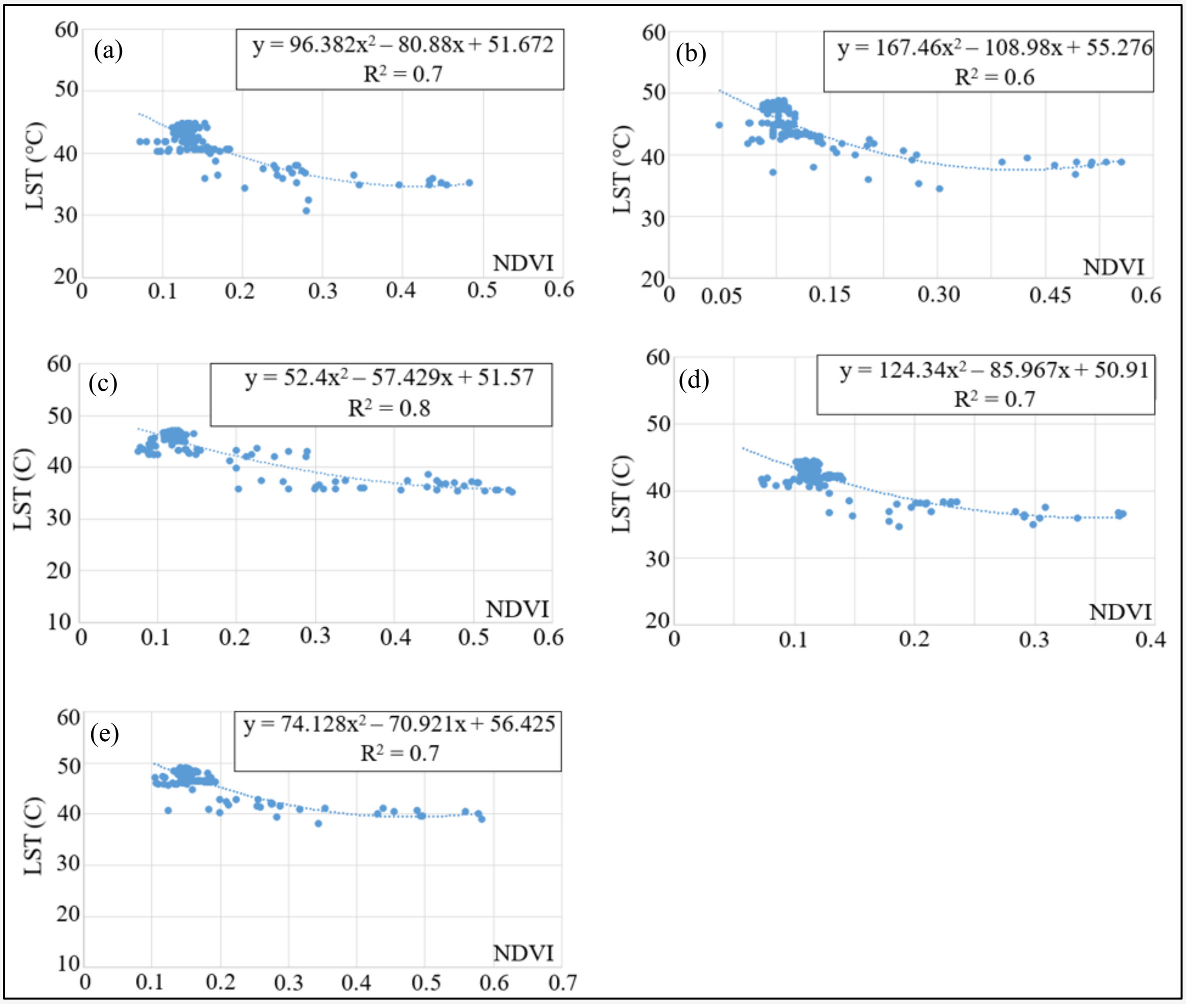

Figure 9: The polynomial correlations between LST-NDVI for the years: (a) 2010, (b) 2011, (c) 2013, (d) 2016 and (e) 2018

The first category, marked in dark green and reflecting a UHI value of zero, suggests no sign of the heat island effect. This area typically includes agricultural land and bodies of water, remaining consistent throughout all the study years. On the other hand, the second category, highlighted in light green, indicates a slight heat island effect, often found in regions with sparse or less dense vegetation.

The third category, shown in orange, highlights a moderate heat island effect primarily linked to urban areas. When we look at the UHI maps from 2010 and 2018, it's clear that this zone has expanded significantly, especially in the southwestern part of Sunland Park. This growth seems closely connected to the urban development that has taken place in that area, as reflected in the land use and land cover classification results.

The fourth category, highlighted in red, represents areas with the strongest surface UHI intensity. These areas were mainly associated with extensive exposed barren soils and sparsely vegetated rangelands, which exhibited higher daytime surface temperatures because the lack of vegetation and limited soil moisture reduced evapotranspiration, allowing a greater proportion of the absorbed solar energy to be converted into sensible heat. In addition, differences in surface albedo, emissivity, and aerodynamic roughness may have contributed to the observed spatial variations in surface temperature. In 2010, this category occupied a larger area than in 2018. This reduction coincides with the conversion of portions of rangeland into urban land.

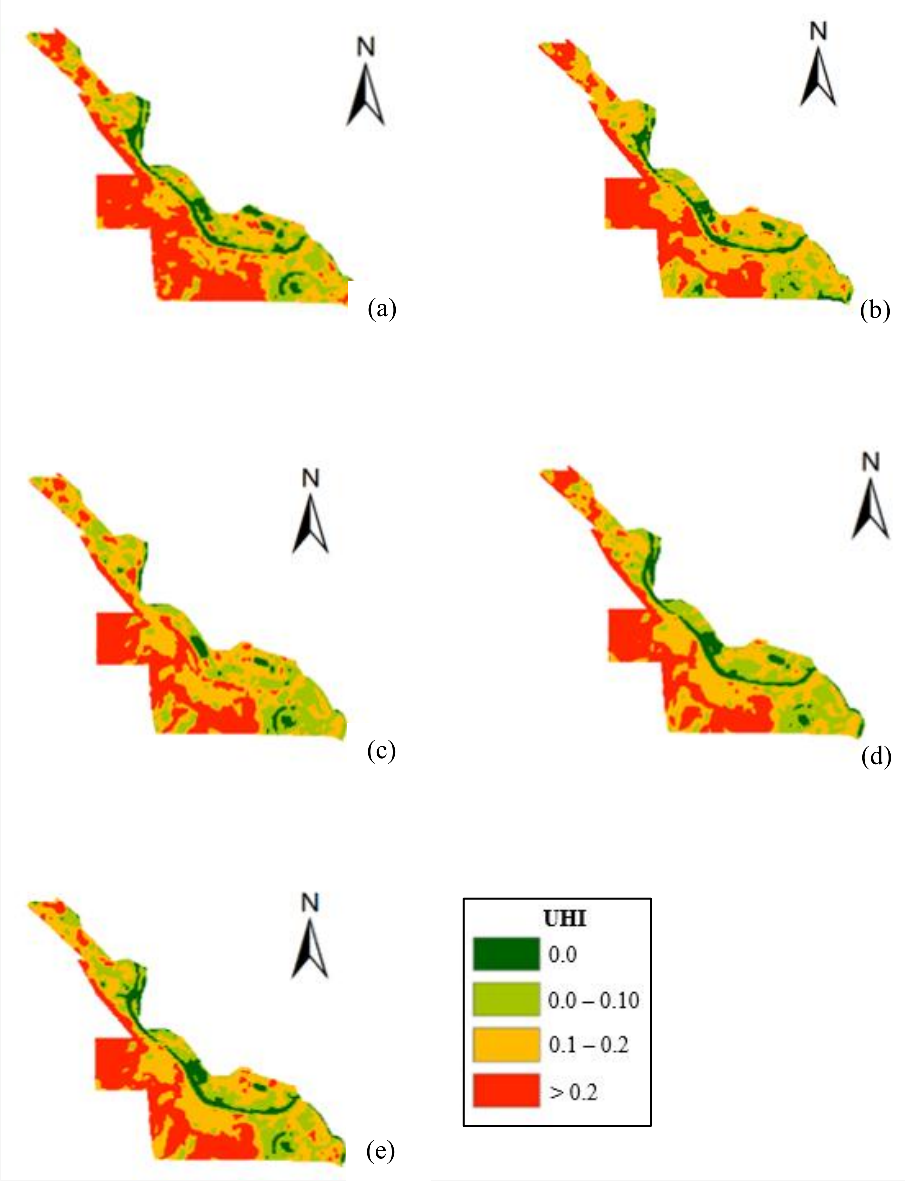

Figure 10: Urban heat island: (a) 2010, (b) 2011, (c) 2013, (d) 2016, and (e) 2018

Although urban surfaces generally absorb and store considerable amounts of heat, the relatively lower daytime surface temperatures observed in some newly developed urban areas may be associated with irrigated vegetation, shading, and differences in surface characteristics compared with the surrounding exposed barren soils. Therefore, the observed reduction in the highest UHI category should be interpreted as being associated with local land-cover characteristics rather than as evidence that urbanization generally reduces surface temperatures in arid environments.

Even though the rangeland areas have shrunk, they still show the highest intensity of Urban Heat Island (UHI) effects, with a maximum index value of 0.2. This finding is backed by land surface temperature (LST) measurements. In 2018, urban regions reached LST values between about 47 to 50 °C, while exposed soil surfaces were even hotter, soaring to temperatures from 50 to 55 °C. In contrast, vegetation and water bodies consistently recorded the lowest LST values, ranging between approximately 34 and 42 °C for the same year. These temperature ranges are consistent with the spatial distribution of UHI classes and land cover types, reinforcing the strong influence of land surface characteristics on UHI intensity in this arid urban environment.

ISSN: 1686-6576 (Printed) | ISSN 2673-0014 (Online) | © Geoinformatics International

3.7 Suggestion for Improvement Strategies for Surface Temperature

The findings of this analysis suggest that Sunland Park may benefit from implementing mitigation strategies to reduce daytime land surface temperatures while considering the limited water resources typical of arid environments. Expanding urban vegetation through trees, shrub, and grass planting may help reduce surface temperatures by providing shade and enhancing evapotranspiration. Increasing urban green spaces may contribute to thermal regulation while also providing additional environmental benefits, including improved air quality, enhanced visual appeal, and ecosystem services. The expansion of vegetation across land surfaces leads to reduced solar radiation exposure to Earth's surface which results in lower heat absorption. The city may benefit from restoring and maintaining urban vegetation because this practice can enhance wildlife habitats, improve water quality, and contribute to a more environmentally sustainable urban environment. Native drought-resistant plant species should be used in dry areas because they need minimal watering to survive while delivering important ecological and thermal advantages. These measures may also provide additional economic and environmental benefits because properties will increase in value and residential areas will become more desirable. Water bodies are known to exert a cooling influence on surrounding areas; however, Sunland Park relies primarily on the Rio Grande as a limited surface water source. Where water resources permit, small artificial or reclaimed water features may provide localized cooling effects.

However, because Sunland Park is located in an arid region with limited water availability, any water-based cooling strategy should prioritize sustainability and efficient water use. The interventions require strategic planning to reach their highest water efficiency potential while sustaining operational sustainability. The findings from this research reveal that barren soils and sparsely vegetated rangelands tend to have higher daytime land surface temperatures compared to many urban areas. This difference underscores the significant role that land cover characteristics play in shaping thermal patterns, especially in arid environments. These temperature variations can largely be attributed to the surface energy balance linked to different land cover types. Vegetated areas are able to dissipate a significant amount of the solar energy they absorb through a process called evapotranspiration. This mechanism reduces the sensible heat flux, ultimately lowering the surface temperature. In contrast, barren soils, which typically have limited soil moisture, experience restricted evaporative cooling. As a result, a greater proportion of the absorbed energy is transformed into sensible heat, raising their surface temperatures. Interestingly, some urban areas show relatively lower land surface temperatures. This may be due to factors such as the presence of irrigated vegetation, shading effects, specific land management practices, and the unique characteristics of urban surfaces.

However, it's important to note that this work did not quantify these factors explicitly. Thus, while these explanations are plausible, they should be viewed as interpretations rather than confirmed mechanisms. Future research that incorporates a broader range of indicators such as the Normalized Difference Built-up Index (NDBI), surface albedo, fractional vegetation cover, impervious surface fraction, or proxies for soil moisture could offer a more detailed understanding of what drives land surface temperatures in arid urban contexts. It's also worth mentioning that urban materials like asphalt and concrete typically have a higher capacity for thermal storage compared to vegetated surfaces, allowing them to retain heat throughout the day. However, in the arid climate of Sunland Park, extensive areas of exposed barren soil may actually reach even higher daytime temperatures due to their limited soil moisture and reduced capacity for evaporative cooling. To combat the accumulation of heat in urban environments, utilizing high-albedo (reflective) materials in construction, along with permeable surfaces, can significantly reduce the absorption of solar energy and heat storage. This approach not only helps mitigate excessive daytime heat but can also enhance overall thermal comfort in urban settings.

This analysis examines daytime land surface temperatures derived from Landsat imagery acquired during the satellite overpass. Consequently, the results represent daytime surface thermal patterns rather than the complete diurnal urban heat island cycle. The thermal behavior of urban materials differs substantially between day and night because materials such as concrete, asphalt, and masonry possess high thermal mass, allowing them to absorb solar energy during the day and gradually release it after sunset. Therefore, nighttime urban heat island characteristics may differ from the daytime surface thermal patterns reported in this work. Future research should integrate daytime and nighttime thermal observations, together with ground-based air-temperature measurements, to provide a more comprehensive assessment of urban heat island dynamics in arid environments.

ISSN: 1686-6576 (Printed) | ISSN 2673-0014 (Online) | © Geoinformatics International

4. Conclusion

The present work investigates the impact of urbanization-related changes in land use and land cover (LULC) on land surface temperature (LST) and the characteristics of the urban heat island (UHI) effect in Sunland Park, New Mexico, which is located in an arid urban environment. By analyzing five Landsat images taken in May of the years 2010, 2011, 2013, 2016, and 2018, the research tracks transformations in urban development, vegetation cover, and surface temperature patterns throughout the daytime. Over the analyzed period, urban land expanded by approximately 15%, while rangeland decreased by around 18%. This trend reflects the ongoing changes in the landscape as the city continues to grow. The analysis revealed that exposed barren soils and sparsely vegetated rangelands typically exhibited the highest daytime surface temperatures. Interestingly, some urban areas displayed lower LST than the surrounding barren lands. This observation does not suggest that urbanization inherently reduces surface temperatures; rather, it indicates that thermal conditions in arid settings are heavily influenced by factors such as the type of land cover, vegetation density, soil moisture levels, and local land management practices. The study also identified an inverse relationship between the Normalized Difference Vegetation Index (NDVI) and LST, underscoring the cooling effects that vegetation has through shading and evapotranspiration. Notably, the most intense surface UHI effects were often linked to exposed barren land rather than densely populated urban areas when examining the selected images

These findings highlight that the response of land to urbanization in arid and semi-arid environments is not solely dependent on the growth of built environments but is also significantly influenced by the pre-existing land conditions and subsequent management practices. Enhancing vegetation cover, developing green infrastructure, and implementing water-efficient landscaping could mitigate daytime surface heating and enhance thermal resilience in urban areas. While this analysis relies on data from only five Landsat images taken in May, thus limiting its year-round thermal behavior insights, the conclusions drawn offer valuable guidance for urban planners and environmental managers aiming to establish more sustainable land-use practices in arid cities.

References

[1] Jiang, Y., Fu, P. and Weng, Q., (2015). Assessing the Impacts of Urbanization-Associated Land Use/Cover Change on Land Surface Temperature and Surface Moisture: A Case Study in the Midwestern United States. *Remote Sensing,* Vol. 7; 4880-4898. https://doi.org/10.3390/rs70404880.

[2] Carlson, T., N. and Arthur, S., T., (2000). The Impact of Land Use-Land Cover Changes due to Urbanization on Surface Microclimate and Hydrology: A Satellite Perspective. *Global and Planetary Change,* Vol. 25; 49-65. https://doi.org/10.1016/S0921-8181(00)00021-7.

[3] Shalaby, A. and Tateishi, R., (2007). Remote Sensing and GIS for Mapping and Monitoring Land Cover and Land-Use Changes in the Northwestern Coastal Zone of Egypt. *Applied Geography,* Vol. 27; 28-41. https://doi.org/10.1016/j.apgeog.2006.09.004.

[4] Jensen, J. R., (2015). *Introductory Digital Image Processing: A Remote Sensing Perspective.* Fourth ed. Prentice-Hall, Upper Saddle River, New Jersey.

[5] Fabrizi, R., Bonafoni, S. and Biondi, R., (2010). Satellite and Ground-Based Sensors for the Urban Heat Island Analysis in the City of Rome. *Remote Sensing,* Vol. 2; 1400-1415. https://doi.org/10.3390/rs2051400.

[6] Camps-Valls, G., Marsheva, T. V. B. and Zhou, D., (2007). Semi-Supervised Graph-Based Hyperspectral Image Classification. *IEEE Transactions on Geoscience and Remote Sensing,* Vol. 45; 3044-3054. https://doi.org/10.1109/TGRS.2007.895416.

[7] Karan, S. K. and Samadder, S. R., (2016). Accuracy of Land Use Change Detection using Support Vector Machine and Maximum Likelihood Techniques for Open-Cast Coal Mining Areas. *Environmental Monitoring and Assessment,* Vol. 188. https://doi.org/10.1007/s10661-016-5494-x.

[8] Lu, D., Mausel, P., Brondízio, E. and Moran, E., (2004). Change Detection Techniques. *International Journal of Remote Sensing,* Vol. 25; 2365-2401. https://doi.org/10.1080/0143116031000139863.

[9] Willis, K., (2015). Remote Sensing Change Detection for Ecological Monitoring in United States Protected Areas. *Biological Conservation,* Vol. 182; 233-242. https://doi.org/10.1016/j.biocon.2014.12.006.

[10] Imhoff, M. L., Zhang, P., Wolfe, R. E. and Bounoua, L., (2010). Remote Sensing of the Urban Heat Island Effect across Biomes in the

Continental USA. *Remote Sensing of Environment,* Vol. 114; 504-513. https://doi.org/10.1016/j.rse.2009.10.008.

[11] Abutaleb, K., Ngie, A., Darwish, A., Ahmed, M., Arafat, S. and Ahmed, F., (2015). Assessment of Urban Heat Island using Remotely Sensed Imagery over Greater Cairo, Egypt. *Advances in Remote Sensing,* Vol. 4. https://doi.org/10.4236/ars.2015.41004.

[12] Berardi, U., GhaffarianHoseini, A. and GhaffarianHoseini, A., (2014). State-of-the-Art Analysis of the Environmental Benefits of Green Roofs. *Applied Energy,* Vol. 115; 411-428. https://doi.org/10.1016/j.apenergy.2013.10.047.

[13] Saiz, S., Kennedy, C., Bass, B. and Pressnail, K., (2006). Comparative Life Cycle Assessment of Standard and Green Roofs. *Environmental Science & Technology,* Vol. 40(13); 4312-4316. https://doi.org/10.1021/es0517522.

[14] Kim, J., Hong, T. and Koo, C. W., (2012). Economic and Environmental Evaluation Model for Selecting the Optimum Design of Green Roof Systems in Elementary Schools. *Environmental Science & Technology,* Vol. 46(15); 8475-8483. https://doi.org/10.1021/es2043855.

[15] Rouse, Jr. J. W., Haas, R. H., Schell, J. A. and Deering, D. W., (1973). Monitoring the Vernal Advancement and Retrogradation (Green Wave Effect) of Natural Vegetation. *NASA/GSFC Type III Final Report.* [Online]. Available: https://ntrs.nasa.gov/citations/19740004927. [Accessed: Mar. 30, 2021].

[16] Weng, Q., Lu, D. and Schubring, J., (2004). Estimation of Land Surface Temperature-Vegetation Abundance Relationship for Urban Heat Island Studies. *Remote Sensing of Environment,* Vol. 89; 467-483. https://doi.org/10.1016/j.rse.2003.11.005.

[17] Ferrelli, F., Cisneros, M. A. H., Delgado, A. L. and Piccolo, M. C., (2018). Spatial and Temporal Analysis of the LST-NDVI Relationship for the Study of Land Cover Changes and their Contribution to Urban Planning in Monte Hermoso, Argentina. *Documents d'Anàlisi Geogràfica,* Vol. 64; 25-47. https://doi.org/10.5565/rev/dag.355.

[18] Thammaboribal, P. (2024). Investigating Land Surface Temperature Variation and Land Use Land Cover Changes in Pathumthani, Thailand (1997-2023) using Landsat Satellite Imagery: A Comprehensive Analysis of LST and Urban Hot Spots (UHS). *International Journal of Geoinformatics*, Vol. 20(2); 27–41. https://doi.org/10.52939/ijg.v20i2.3063.

[19] Jiménez-Muñoz, J. C. and Sobrino, J. A., (2003). A Generalized Single-Channel Method for Retrieving Land Surface Temperature from Remote Sensing Data. *Journal of Geophysical Research: Atmospheres,* Vol. 108. https://doi.org/10.1029/2003JD003480.

[20] Sobrino, J. A., Jimenez-Munoz, J. C. and Paolini, L., (2004). Land Surface Temperature Retrieval from Landsat TM 5. *Remote Sensing of Environment,* Vol. 90; 434-440. https://doi.org/10.1016/j.rse.2004.02.003.

[21] Sunland Park Comprehensive Qualitative Community Assessment. (2005). University of Texas at El Paso, Social Work Program, Kip Coggins, PhD., Contributors: Co-editor Natalia Medina Coggins.

[22] US Census Bureau. (2010). People QuickFacts. Sunland Park City, Doña Ana County, New Mexico, and the United States. [Online]. Available: https://www.census.gov/quickfacts/fact/table/sunlandparkcitynewmexico. [Accessed: April 20, 2022].

[23] US Census Bureau. (2017). *People QuickFacts. Sunland Park City, Doña Ana County, New Mexico, and the United States.* [Online]. Available: https://www.census.gov/quickfacts/fact/table/sunlandparkcitynewmexico. [Accessed: April 20, 2022].

[24] USGS. (n.d.). EarthExplorer. U.S. Geological Survey. [Online]. Available: https://earthexplorer.usgs.gov/. [Accessed: May 22, 2020].

[25] Sawalhah, M. N., Al-Kofahi, S. D., Othman, Y. A. and Cibils, A. F., (2018). Assessing Rangeland Cover Conversion in Jordan after the Arab Spring using a Remote Sensing Approach. *Journal of Arid Environments,* Vol. 157; 97-102. https://doi.org/10.1016/j.jaridenv.2018.07.003.

[26] Kawata, Y., Ohtani, A., Kusaka, T. and Ueno, S., (1990). Classification of the Pearl River Delta using the MOS-1 MESSR Data before and after the Atmospheric Correction. *IEEE Transactions on Geoscience and Remote Sensing,* Vol. 28; 755-760. https://doi.org/10.1109/TGRS.1990.573015.

[27] Kaufman, Y. J. and Sendra, C., (1988). Algorithm for Automatic Atmospheric Corrections to Visible and Near-IR Satellite Imagery. *International Journal of Remote Sensing,* Vol. 9; 1357-1381. https://doi.org/10.1080/01431168808954942.

[28] Chavez, P. S., (1996). Image-Based Atmospheric Corrections-Revisited and

Improved. *Photogrammetric Engineering and Remote Sensing,* Vol. 62; 1025-1036.

[29] Chavez, P. S. Jr., (1975). Atmospheric, Solar, and M.T.F. Corrections for ERTS Digital Imagery. *Proceedings of the American Society of Photogrammetry Fall Conference, Phoenix*, Arizona.

[30] Chavez, Jr. P. S., (1988). An Improved Dark-Object Subtraction Technique for Atmospheric Scattering Correction of Multispectral Data. *Remote Sensing of Environment,* Vol. 24; 459-479. https://doi.org/10.1016/0034-4257(88)90019-3.

[31] Chavez Jr. P. S., (1989). Radiometric Calibration of Landsat Thematic Mapper Multispectral Images. *Photogrammetric Engineering and Remote Sensing,* Vol. 55; 1285-1294.

[32] Song, C., Woodcock, C. E., Seto, K. C., Lenney, M. P. and Macomber, S. A., (2001). Classification and Change Detection Using Landsat TM Data: When and How to Correct Atmospheric Effects? *Remote Sensing of Environment,* Vol. 75; 230-244. https://doi.org/10.1016/S0034-4257(00)00169-3.

[33] Thammaboribal, P., and Tripathi, N. (2024). Predicting Land Use and Land Cover Changes in Pathumthani, Thailand: A Comprehensive Analysis from 2013 to 2023 Using Landsat Satellite Imagery and CA-ANN Algorithm, with Projections for 2028 and 2038. *International Journal of Geoinformatics*, Vol. 20(5); 13–27. https://doi.org/10.52939/ijg.v20i5.3225.

[34] Anderson, J. R., Hardy, E. E., Roach, J. T. and Witmer, R. E., (1976). *A Land Use and Land Cover Classification System for Use with Remote Sensor Data.* U.S. Geological Survey Professional Paper 964. [Online]. Available: https://pubs.usgs.gov/pp/0964/report.pdf. [Accessed: Nov. 30, 2020].

[35] USDA NASS. (n.d.). *CropScape - Cropland Data Layer. National Agricultural Statistics Service, Geospatial Data Gateway.* [Online]. Available: https://nassgeodata.gmu.edu/CropScape/. [Accessed: Nov. 11, 2020].

[36] Jensen, J. R., (2005). *Introductory Digital Image Processing: A Remote Sensing Perspective.* Third ed. Prentice-Hall, Upper Saddle River, New Jersey.

[37] Chen, D. and Stow, D., (2002). The Effect of Training Strategies on Supervised Classification at Different Spatial Resolutions. *Photogrammetric Engineering and Remote Sensing,* Vol. 68; 1155-1162.

[38] Stehman, S., (1996). Estimating the Kappa Coefficient and Its Variance under Stratified Random Sampling. *Photogrammetric Engineering and Remote Sensing,* Vol. 62; 401-407.

[39] Verbyla, D. L. and Hammond, T. O., (1995). Conservative Bias in Classification Accuracy Assessment due to Pixel-by-Pixel Comparison of Classified Images with Reference Grids. *Remote Sensing,* Vol. 16; 581-587. https://doi.org/10.1080/01431169508954424.

[40] Congalton, R. G. and Green, K., (2009). *Assessing the Accuracy of Remotely Sensed Data: Principles and Practices.* CRC Press, Boca Raton, Florida.

[41] Carfagna, E. and Gallego, F. J., (2005). Using Remote Sensing for Agricultural Statistics. *International Statistical Review,* Vol. 73; 389-404. https://doi.org/10.1111/j.1751-5823.2005.tb00155.x.

[42] Skoković, D., Sobrino, J. A., Jimenez-Munoz, J. C., Soria, G., Jušien, Y., Mattar, C. and Cristóbal, J., (2014). *Calibration and Validation of Land Surface Temperature for Landsat 8-TIRS Sensor.* LPVE (Land Product Validation and Evolution).

[43] Price, J. C., (1984). Land Surface Temperature Measurements from the Split Window Channels of the NOAA 7 Advanced Very High-Resolution Radiometer. *Journal of Geophysical Research: Atmospheres,* Vol. 89; 7231-7237. https://doi.org/10.1029/JD089iD05p07231.

[44] Kerr, Y. H., Lagouarde, J. P., and Imbernon, J., (1992). Accurate Land Surface Temperature Retrieval from AVHRR Data with Use of an Improved Split Window Algorithm. *Remote Sensing of Environment,* Vol. 41; 197-209. https://doi.org/10.1016/0034-4257(92)90078-X.

[45] Thammaboribal, P., Triapthti, N., and Lipiloet, S. (2025). Comparative Analysis of Land Surface Temperature (LST) Retrieved from Landsat Level 1 and Level 2 Data: A Case Study in Pathumthani Province, Thailand. *International Journal of Geoinformatics*, Vol. 21(4), 160–177. https://doi.org/10.52939/ijg.v21i4.4089.

[46] Sobrino, J. A., Li, Z. L., Stoll, M. P. and Becker, F., (1994). Improvements in the Split-Window Technique for Land Surface Temperature Determination. *IEEE Transactions on Geoscience and Remote Sensing,* Vol. 32; 243-253. https://doi.org/10.1109/36.295038.

[47] François, C. and Ottlé, C., (1996). Atmospheric Corrections in the Thermal Infrared: Global and Water Vapor Dependent Split-Window

Algorithms-Applications to ATSR and AVHRR Data. *IEEE Transactions on Geoscience and Remote Sensing,* Vol. 34; 457-470. https://doi.org/10.1109/36.485123.

[48] Du, C., Ren, H., Qin, Q., Meng, J. and Zhao, S., (2015). A Practical Split-Window Algorithm for Estimating Land Surface Temperature from Landsat 8 Data. *Remote Sensing,* Vol. 7; 647-665. https://doi.org/10.3390/rs70100647.

[49] Weiss, J. L., Gutzler, D. S., Coonrod, J. E. A. and Dahm, C. N., (2004). Long-Term Vegetation Monitoring with NDVI in a Diverse Semi-Arid Setting, Central New Mexico, USA. *Journal of Arid Environments,* Vol. 58; 249-272. https://doi.org/10.1016/j.jaridenv.2003.07.001.

[50] Jiang, Z., Huete, A. R., Li, J. and Chen, Y., (2006). An Analysis of Angle-Based with Ratio-Based Vegetation Indices. *IEEE Transactions on Geoscience and Remote Sensing,* Vol. 44; 2506-2513. https://doi.org/10.1109/TGRS.2006.873205.

[51] Wang, F., Qin, Z., Song, C., Tu, L., Karnieli, A. and Zhao, S., (2015). An Improved Mono-Window Algorithm for Land Surface Temperature Retrieval from Landsat 8 Thermal Infrared Sensor Data. *Remote Sensing,* Vol. 7; 4268-4289.https://doi.org/10.3390/rs70404268

[52] Sobrino, J. A., Jiménez-Muñoz, J. C., Sòria, G., Romaguera, M., Guanter, L., Moreno, J. and Martínez, P., (2008). Land Surface Emissivity Retrieval from Different VNIR and TIR Sensors. *IEEE Transactions on Geoscience and Remote Sensing,* Vol. 46; 316-327. https://doi.org/10.1109/TGRS.2007.904834.

[53] Giannini, M. B., Belfiore, O. R., Parente, C. and Santamaria, R., (2015). Land Surface Temperature from Landsat 5 TM Images: Comparison of Different Methods using Airborne Thermal Data. *Journal of Engineering Science and Technology Review,* Vol. 8. https://doi.org/10.25103/jestr.083.11.

[54] Agbor, C. F. and Makinde, E. O., (2018). Land Surface Temperature Mapping using Geoinformation Techniques. *Geoinformatics FCE CTU Journal,* Vol. 17; 17-32. https://doi.org/10.14311/gi.17.1.2.

[55] Barsi, J. A., Markham, B. L., Montanaro, M., Gerace, A., Hook, S. J., Schott, J. R., Raqueno, N. G. and Morfitt, R., (2017). Landsat-8 Thermal Infrared Sensor (TIRS) Vicarious Radiometric Calibration. *Remote Sensing,* Vol. 9(11). https://doi.org/10.3390/rs9111171.

[56] Yu, X., Guo, X. and Wu, Z., (2014). Land Surface Temperature Retrieval from Landsat 8 TIRS-Comparison between Radiative Transfer Equation-Based Method, Split Window Algorithm and Single Channel Method. *Remote Sensing,* Vol. 6; 9829-9852. https://doi.org/10.3390/rs6109829.

[57] Coll, C., Niclòs, R., Puchades, J., García-Santos, V., Galve, J. M., Pérez-Planells, L., Valor, E. and Theocharous, E., (2019). Laboratory Calibration and Field Measurement of Land Surface Temperature and Emissivity using Thermal Infrared Multiband Radiometers. *International Journal of Applied Earth Observation and Geoinformation,* Vol. 78; 227-239. https://doi.org/10.1016/j.jag.2019.02.002.

[58] Zhang, Y., Yu, T., Gu, X., Zhang, Y. and Chen, L., (2006). Land Surface Temperature Retrieval from CBERS-02 IRMSS Thermal Infrared Data and Its Applications in Quantitative Analysis of Urban Heat Island Effect. *Journal of Remote Sensing-Beijing,* Vol. 10. https://www.ygxb.ac.cn/en/article/doi/10.11834/jrs.200605117.

[59] Jagtap, A., Shedge, D., and Mane, P. (2024). Exploring the Effects of Land Use/Land Cover (LULC) Modifications and Land Surface Temperature (LST) in Pune, Maharashtra with Anticipated LULC for 2030. *International Journal of Geoinformatics*, Vol. 20(2), 42–63. https://doi.org/10.52939/ijg.v20i2.3065.

[60] Smith, A., Wooster, M., Powell, A. and Usher, D., (2002). Texture Based Feature Extraction: Application to Burn Scar Detection in Earth Observation Satellite Sensor Imagery. *International Journal of Remote Sensing,* Vol. 23; 1733-1739. https://doi.org/10.1080/01431160110106104.

[61] Stehman, S. V. and Foody, G. M., (2019). Key Issues in Rigorous Accuracy Assessment of Land Cover Products. *Remote Sensing of Environment,* Vol. 231. https://doi.org/10.1016/j.rse.2019.05.018.

[62] Tawalbeh, Z. M., Bawazir, A. S., Fernald, A. and Sabie, R., (2024). Spatiotemporal Variabilities in Evapotranspiration of Alfalfa: A Case Study Using Remote Sensing METRIC and SSEBop Models and Eddy Covariance. *Remote Sensing,* Vol. 16(13). https://doi.org/10.3390/rs16132290.

[63] Yue, W., Xu, J., Tan, W. and Xu, L., (2007). The Relationship between Land Surface Temperature and NDVI with Remote Sensing: Application to Shanghai Landsat 7 ETM+ Data. *International Journal of Remote Sensing,* Vol. 28; 3205-3226. https://doi.org/10.1080/01431160500306906.